

Article

# Adaptive Flight Path Control of Airborne Wind Energy Systems

Tarek Dief<sup>1,†,‡</sup> , Uwe Fechner<sup>2,‡</sup>, Roland Schmehl<sup>3,‡,\*</sup> , Shigeo Yoshida<sup>4</sup>  and Mostafa A. Rushdi<sup>5,6</sup> 

<sup>1</sup> Post-doctoral Fellow, RIAM, 6-1, Kasuga, Kyushu University, Fukuoka, Japan; tarek.na3em@riam.kyushu-u.ac.jp

<sup>2</sup> Aenarete - Wind Drones, The Hague, 2522 DT, The Netherlands; fechner@aenarete.eu

<sup>3</sup> Associate Professor, Delft University of Technology, 2629 HS Delft, The Netherlands; r.schmehl@tudelft.nl

<sup>4</sup> Professor, RIAM, 6-1, Kasuga, Kyushu University, Fukuoka, Japan; yoshidas@riam.kyushu-u.ac.jp

<sup>5</sup> Ph.D. Candidate, ESST,6-1, Kasuga, Kyushu University, Fukuoka, Japan; rushdimostafa@riam.kyushu-u.ac.jp

<sup>6</sup> Faculty of Engineering and Technology, Future University in Egypt (FUE), 5th Settlement, New Cairo 11835, Egypt; Mostafa.Roshdi@fue.edu.eg

\* Correspondence: r.schmehl@tudelft.nl

**Abstract:** In this paper we apply a system identification algorithm and an adaptive controller to a simple kite system model to simulate crosswind flight maneuvers for airborne wind energy harvesting. The purpose of the system identification algorithm is to handle uncertainties related to a fluctuating wind speed and shape deformations of the tethered membrane wing. Using a pole-placement controller we determine the required locations of the closed-loop poles and then enforce them by adapting the control gains in real time. We compare the path-following performance of the proposed approach with a classical PID controller using the same system model. The capability of the system identification algorithm to recognize sudden changes in the dynamic model or the wind conditions and the ability of the controller to stabilize the system in the presence of such changes are confirmed. Furthermore, the system identification algorithm is applied to determine the parameters of a kite with variable-length tether used in a flight test of the 20 kW kite power system of TU Delft. Experimental data of this test were analyzed using the system identification algorithm in real time and significant changes were observed in the parameters of the dynamic model which strongly affect the resulting response.

**Keywords:** airborne wind energy; kite system; system identification; adaptive algorithms; pole placement

## Nomenclature

### Latin Symbols

$A$	denominator polynomial of the open-loop TF	-
$a_1, a_2, b_1, b_2$	system identification parameters	-
$B$	numerator polynomial of the open-loop TF	-
$s_1, s_2, r_1$	adaptive control parameters	-
$c_1$	steering sensitivity coefficient of the turn rate law	rad/m
$c_2$	gravity sensitivity coefficient of the turn rate law	rad.m/s <sup>2</sup>
$c_0$	steering offset of the turn rate law	-
$G(z^{-1})$	open-loop TF of the model in $z$ -domain	-
$G_c(z^{-1})$	closed-loop TF of the model in $z$ -domain	-
$h_{fig}$	angular height of figure-of-eight maneuver	rad

29	$l_t$	tether length	m
30	$P_3$	angular reference position for the FPP	rad
31	$P_4$	angular reference position for the FPP	rad
32	$n_r$	order of $R$ -polynomial	-
33	$R$	numerator polynomial of the control TF	-
34	$r$	radial coordinate of the kite	m
35	$n_s$	order of $S$ -polynomial	-
36	$S$	denominator polynomial of the control TF	-
37	$U(z^{-1})$	system input which is defined as $u_s$ in $z$ -domain	-
38	$u'_d$	relative depower action	-
39	$u_s$	relative steering action	-
40	$v_{w,ref}$	horizontal wind velocity at the reference height	m/s
41	$x_k, y_k, z_k$	body-fixed reference frame of the kite	-
42	$x_{SE}, y_{SE}, z_{SE}$	small earth reference frame	-
43	$x_w, y_w, z_w$	wind reference frame	-
44	$Y(z^{-1})$	estimated course angle obtained from the system identification in $z$ -domain	rad
45	$y_m$	measured course angle obtained from the sensor	rad
46	$z^{-1}$	backward shift operator in $z$ -domain	-
47	<b>Greek Symbols</b>		
48	$\beta$	elevation angle of the kite	rad
49	$\beta_{sw}$	elevation angle to switch flight mode	rad
50	$\chi$	course angle of the kite	rad
51	$\dot{\chi}$	rate of change of the course angle	rad/s
52	$\dot{\chi}_R$	rate of change of the course angle to fly a turn with radius $R$	rad/s
53	$\chi_{set}$	set value for the course angle	rad
54	$\delta_{min}$	minimal, angular attractor point distance	rad
55	$\omega_{ref}$	reference value of the angular speed	rad/s
56	$w_{fig}$	angular width of figure-of-eight maneuver	rad
57	$\phi$	azimuth angle of the kite	rad
58	$\phi_{c2}$	azimuth angle at point $C_2$	rad
59	$\phi_{set}$	set value of azimuth angle	rad
60	$\phi_{sw}$	azimuth angle to switch flight mode	rad
61	$\psi$	heading angle of the kite	rad
62	$\dot{\psi}$	turn rate of the kite	rad/s
63	$\rho$	turn radius of the trajectory of the kite point <b>K</b>	rad
64	<b>Vectors and Matrices</b>		
65	$\omega$	angular velocity of the kite point <b>K</b> with respect to the origin <b>O</b>	rad/s
66	$\mathbf{P}_{k,set}^{SE}$	position of the kite in angular coordinates( $\phi, \beta$ )	rad
67	$\mathbf{P}_k$	covariance matrix of the estimated error	-
68	$\theta$	last vector estimated using the least square estimation algorithm	-
69	$\mathbf{v}_a$	apparent wind speed	m/s
70	$\mathbf{v}_k$	kite velocity	m/s
71	$\mathbf{v}_{k,r}$	radial kite velocity component	m/s
72	$\mathbf{v}_{k,\tau}$	tangential kite velocity component	m/s
73	$\mathbf{X}$	data of old measurement of course angle and control action	-
74	$\mathbf{Y}_m$	measured course angle obtained from the sensor	rad
75	<b>Abbreviation</b>		
76	AWE	Airborne Wind Energy	
77	FPC	Flight Path Control	
78	FPP	Flight Path Planner	
79	HAWT	Horizontal Axis Wind Turbines	
80	KCU	Kite Control Unit	
81	LEI	Leading Edge Inflatable	
82	MSE	Mean Square Error	
83	NDI	Nonlinear Dynamic Inversion	

84 NMPC Nonlinear Model Predictive Control  
 85 PID Proportional-Integral-Derivative  
 86 SI System Identification  
 87 SISO Single-Input Single-Output  
 88 TF Transfer Function

## 89 1. Introduction

90 Airborne wind energy (AWE) is an emerging renewable energy technology which uses flying  
 91 devices that are tethered to the ground [1–3]. Compared to horizontal axis wind turbines (HAWTs),  
 92 AWE systems have a number of distinct advantages in terms of costs, maintenance, operational altitude  
 93 and capacity factor. However, as wind turbines have matured over decades of continuous research  
 94 and development, AWE technologies, which are at a comparatively early stage of development, are  
 95 still considered to be less reliable. For a HAWT, almost 30% of the power is generated by the tip of  
 96 the rotor blades while the rest of the rotor functions mainly as support structure for the crosswind  
 97 motion of the blades [1,2,4]. The rated power of the generator typically determines the installation. For  
 98 the same rated power, an AWE system generally gives a higher annual yield than a HAWT because  
 99 it can operate at a higher capacity factor. The higher capacity factor is a result of the more persistent  
 100 and more steady wind at higher altitude. However, an AWE system also needs more space than a  
 101 HAWT, which increases the costs of an installation. These land surface costs are still quite unknown  
 and responsible for the large differences in expected costs [5,6].

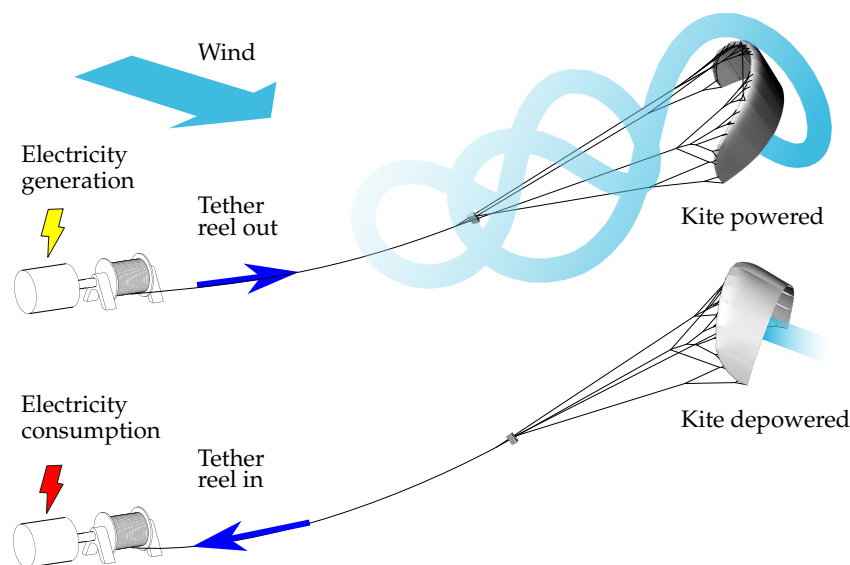


Figure 1. Working principle of the pumping kite power system implemented by TU Delft [5].

102 There are several different concepts and configurations of AWE systems [2,8]. A comparatively  
 103 simple one is the pumping kite power system illustrated in Fig. 1. The kite consists of a flexible  
 104 membrane wing that is steered by a suspended kite control unit (KCU) and tethered to a drum on the  
 105 ground which is coupled to a generator. During reel out of the tether, the kite is operated in crosswind  
 106 figure-of-eight maneuvers, as shown in Fig. 2, to maximize the pulling force and thus generated  
 107 energy when pulling the tether from the drum. When reaching the maximum tether length, the kite is  
 108 depowered and retracted, using the generator as a motor and consuming a fraction of the formerly  
 109 generated energy. The change of the flight patterns between reel-out and reel-in phases results in a net  
 110 energy per pumping cycle [5,9]. The main objective of the control algorithm is to ensure a robust and  
 111 safe flight operation of the kite.  
 112

113 Several mathematical models have been developed to describe the dynamic behavior of the  
 114 kite system [1,3,10,11]. An obvious shortcoming of these models are the numerous idealizations



**Figure 2.** Composite photo of a crosswind figure-of-eight maneuver ( $\Delta t = 1$  s) of a tube kite with 25 m<sup>2</sup> surface area [7].

115 that limit the achievable prediction quality for a flight trajectory in a real wind environment which  
 116 is characterized by local changes in wind speed and direction occurring within seconds [12,13].  
 117 Another modeling challenge is the aeroelastic response of the membrane wing because the substantial  
 118 deformations also majorly affect the aerodynamic properties of the kite system [14–16].

119 Generally, in most control applications, the mathematical model can be based on either: (1) a  
 120 system that has a fixed operating point and control parameters that are fixed due to the stability in the  
 121 model, or (2) a system that has a variable operating point requiring that it is robust enough to sustain  
 122 the variation. The dynamic model representing a kite system is of the latter type since the system  
 123 characteristics are time varying due to the natural fluctuations of the wind environment. This has to be  
 124 considered in the design of the control algorithm for the kite system.

125 In recent years, research on kite control has intensified considerably [17–20]. The developed  
 126 models are typically based on state space representations of the real AWE system, describing the  
 127 nonlinear dynamics of 4 up to 15 states. In [21] the optimal flight path of the kite is determined  
 128 ahead of time, using nonlinear model predictive control (NMPC). However, this control method  
 129 is computationally expensive and with additional expenses for solving the nonlinear optimization  
 130 problem [19,20]. For this reason we consider the method unsuitable for real-time experiments in kite  
 131 applications.

132 Several open source software tools for AWE systems have been developed over the past years  
 133 [11,22,23]. These tools allow the computational simulation of flight maneuvers, virtual testing of flight  
 134 control algorithms and optimizing flight paths in real time. One particular aspect of modeling is the  
 135 flexible tether that is deployed from the ground station and sweeping through the wind field, while  
 136 being exposed to a distributed aerodynamic load and gravity [24]. A common assumption is that of a  
 137 perfectly tensioned, straight tether. While generally valid during the traction phase, this assumption is  
 138 not acceptable during the retraction, landing and take-off phases. Because of the low tension, sagging  
 139 of the tether has to be taken into account in the modeling [9,25].

140 The control approach proposed in [26] is interesting because it does not require any information  
 141 about the kite or the wind field. Although the approach allows high-precision tracking of figure-of-eight  
 142 maneuvers, this is feasible only for a short tether of constant length. The approach is not suitable,  
 143 however, for a long tether or a tether of variable length [12]. The research challenge addressed in this  
 144 work can be summarized as follows:

- 145 • The kite is based on a flexible membrane wing and its shape depends on the aerodynamic force  
146 distribution and structural design and line suspension system.
- 147 • The relative flow velocity experienced by wing and tether varies along the flight path and there  
148 is no accurate way to assess this in real time.
- 149 • An accurate estimation of the wind field is necessary to determine the aerodynamic force  
150 distribution on tether and wing surface [4,5].

151 As a result of this physical complexity the need for robust control to stabilize the kite in real time is  
152 crucial. The challenges mentioned above are addressed as follows:

- 153 • We propose an algorithm that estimates the parameters of the dynamic model of the kite in  
154 real time using system identification (SI) [27–30]. The employed SI algorithm is a non-iterative  
155 technique based on the Plackett’s algorithm due to its ability to calculate the parameters of the  
156 system (dynamic model) with high accuracy without singularity.
- 157 • We further propose an adaptive controller to improve the robustness of the system and stabilize  
158 the kite in different wind conditions. Moreover, SI is considered as a part of the adaptive control  
159 and the estimated parameters are used to obtain the control gains [30], which means that these  
160 gains are updated in real time based on the change in the dynamic model [28].
- 161 • We present a comparison between the adaptive and classical controllers to highlight the  
162 robustness of the controller and the ability of adaptive control to stabilize the kite for different  
163 wind conditions without any change in the SI and adaptive control algorithms.
- 164 • We apply the SI algorithm to experimental data of the 20 kW kite power system of TU Delft [5].  
165 The algorithm is used to estimate the parameters of the system in different operation phases,  
166 such as traction and retraction phases, for two pumping cycles while experiencing changes in  
167 wind speed and tether length.

168 The remainder of this paper is subdivided as follows. Section 2 outlines the components of the  
169 mathematical model and discusses it briefly based on the concepts and implementations described in  
170 [12,28]. The mathematical model includes a simplified kite system model, designed as a single-input  
171 single-output (SISO) model relating the relative steering input (input) to the course angle (output) of  
172 the kite, a flight path planner (FPP) and a flight path controller (FPC). In Sect. 3 the derivation and  
173 implementation of the SI algorithm is discussed in detail. Subsequently, Sect. 4 presents the adaptive  
174 controller based on the estimated parameters from the SI algorithm which is used to stabilize the kite  
175 in real time. In Sect. 5 simulation results are presented for the classical controller described in [12,13,28]  
176 and the combination of adaptive controller and SI algorithm and compared for two different flight  
177 conditions. Finally, Sect. 6 summarizes the experimental results acquired during a flight test of the 20  
178 kW kite power system of TU Delft, then these results are analyzed using the SI algorithm derived in  
179 Sect. 3. Section 7 concludes this article.

## 180 2. Mathematical model

181 The approach presented in this paper has been derived for the 20 kW kite power system of  
182 TU Delft, as illustrated in Figs. 1 and 2. The mathematical model was previously formulated and  
183 demonstrated in [12,28]. The flight path planning (FPP) and flight path control (FPC) approaches  
184 are both designed on the basis of this model. The presented simulation results were obtained by a  
185 Simulink/MATLAB<sup>®</sup> implementation.

### 186 2.1. Simplified kite system model

To describe the flight motion of the kite power system we introduce the wind reference frame  
( $x_w, y_w, z_w$ ), the kite reference frame ( $x_k, y_k, z_k$ ) and the small earth reference frame ( $x_{SE}, y_{SE}, z_{SE}$ ), as  
illustrated in Fig. 3. The wind reference frame is attached to the tether exit point **O** at the ground  
station and rotates with the wind around its  $z_w$ -axis such that its  $x_w$ -axis is always aligned with  
the instantaneous wind direction. It is assumed that this rotation is slow compared to the flight

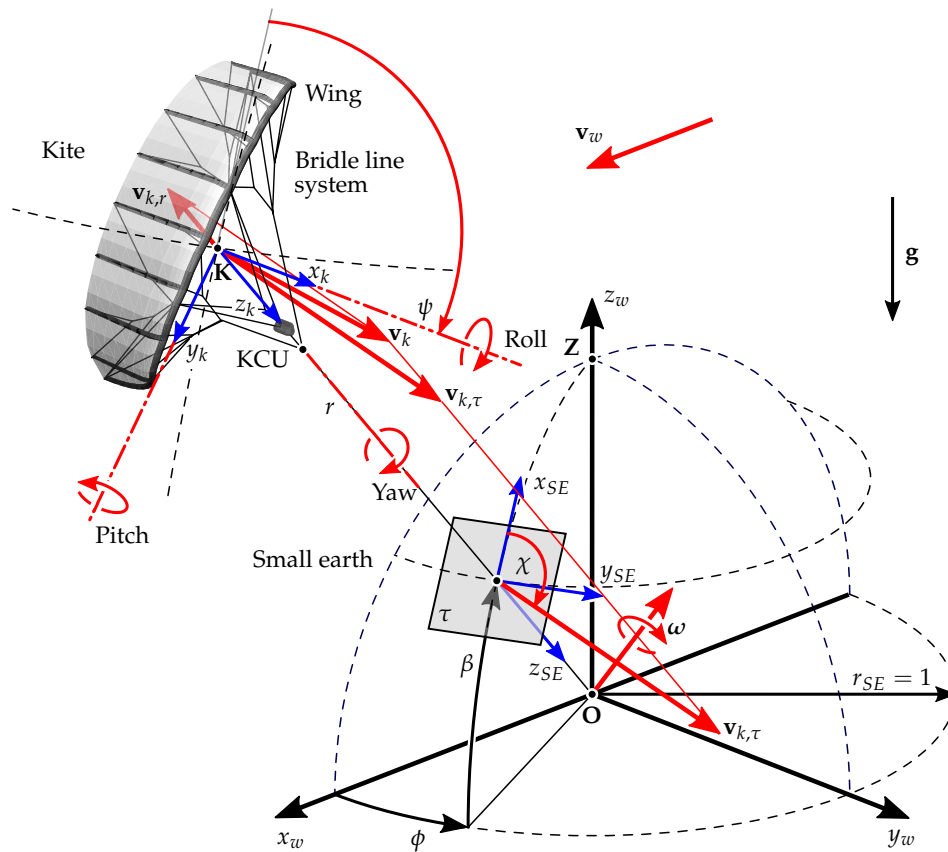


**Figure 3.** Reference frames to describe tethered flight, heading angle  $\psi$  and course angle  $\chi$  of the kite.

dynamics of the kite such that any induced forces can be neglected. The body-fixed kite reference frame is attached to the center of mass  $\mathbf{K}$  of the kite and accounts for wing, bridle line system and the suspended kite control unit (KCU). To obtain the coordinates of the kite in the small earth reference frame [31], its position is projected radially onto the unit sphere around the tether exit point  $\mathbf{O}$ . On the unit sphere we define a local tangential plane  $\tau$ . The position of the kite in the small earth reference frame can be described by the azimuth angle  $\phi$  and the elevation angle  $\beta$ , which represent the latitude and longitude of the position. The velocity  $\mathbf{v}_k$  of the kite can be decomposed into a radial component  $\mathbf{v}_{k,r}$  and a tangential component  $\mathbf{v}_{k,\tau}$  which can be derived from the kite position as

$$v_{k,r} = \dot{r}, \quad (1)$$

$$v_{k,\tau} = r \sqrt{\dot{\phi}^2 \cos^2 \beta + \dot{\beta}^2}. \quad (2)$$

The course angle  $\chi$  is defined as the angle between  $\mathbf{v}_{k,\tau}$  and the upwards direction, represented by the local  $x_{SE}$ -axis [12,13]. The heading angle describes the orientation of the kite in the tangential plane and is defined as the angle between the  $x_k$ -axis and the upwards direction. The course angle  $\chi$  generally follows the heading angle  $\psi$  with a varying offset due to gravity. The angular velocity  $\omega$  of the kite with respect to the origin  $\mathbf{O}$  is kinematically coupled to the tangential velocity of the kite

$$\mathbf{v}_{k,\tau} = \omega \times \mathbf{r}, \quad (3)$$

$$v_{k,\tau} = r\omega, \quad (4)$$

where  $\mathbf{r}$  is the vector pointing from origin  $\mathbf{O}$  to kite  $\mathbf{K}$ . The relative flow velocity at the kite is computed from the wind and kite velocity vectors as

$$\mathbf{v}_a = \mathbf{v}_w - \mathbf{v}_k. \quad (5)$$

187 To simplify the flight path planning (FPP) and flight path control (FPC) implementation we  
188 introduce the following assumptions, which are valid for the traction phase when the tether is generally  
189 fully tensioned:

- 190 • The tether is straight and the tether length is identical to the radial position  $r$  of the kite  $\mathbf{K}$ .
- 191 • The wing is attached to the tether with a bridle line system which constrains the roll and the  
192 pitch of the wing. Only the heading angle  $\psi$  remains as a degree of freedom to control the course  
193 of the kite.
- 194 • The difference between heading and course angles can be neglected. Both angles and their time  
195 derivatives are assumed to be identical in this study.

196 By decomposing the kite velocity into radial and tangential components we essentially decouple  
197 the flight control of the kite from the winch control. The kite is steered by actuation of the rear bridle  
198 line system, which is quantified by the relative steering  $u_s$  that can vary between -1 and 1. Additional  
199 inputs for the kite model are the magnitude of the apparent wind speed  $v_a$ , the initial elevation angle  
200  $\beta_0$ , the angular speed  $\omega$  and the initial values for the course angle  $\chi_0$  and the azimuth angle  $\phi_0$ . The  
201 outputs for this model are the course angle  $\chi$ , its time derivative  $\dot{\chi}$  and the position of the kite in terms  
202 of elevation angle  $\beta$  and azimuth angle  $\phi$ .

To calculate the angular speed  $\omega$  of the kite we use the simplified kite system model that was derived in [12]. In this model, which has also been used in [28], it is assumed that the angular speed  $\omega$  is a function of the elevation angle  $\beta$  only. The angular speed is zero at the maximum value  $\beta_{max}$  and increases linearly with decreasing elevation angle, until it reaches a specific value  $\omega_{ref}$  at  $\beta_{min}$ . This behavior is described by the following correlation

$$\omega = \frac{\beta_{max} - \beta}{\beta_{max} - \beta_{min}} \omega_{ref}. \quad (6)$$

Flight tests of the TU Delft Hydra kite [5,9] have shown that the maximum elevation angle  $\beta_{max} = 73^\circ$  is reached when the kite is positioned statically at a tether length of 300 m at an approximate ground wind speed of 6 m/s. We further assume that the value  $\omega_{ref}$  is a linear function of the apparent wind speed  $v_a$ , which can be expressed as

$$\omega_{ref} = \frac{v_a}{v_{a,0}} \omega_{ref,0}, \quad (7)$$

203 where  $\omega_{ref,0}$  denotes the angular speed that is reached at a specific apparent wind speed  $v_{a,0}$ . From  
204 the flight tests we find an angular speed  $\omega_{ref,0} = 5$  deg/s for an elevation angle  $\beta_{min} = 22^\circ$  and an  
205 apparent wind velocity  $v_{a,ref} = 20$  m/s. Combining Eqs. (6) and (7) we can calculate the angular speed  
206  $\omega$  of the kite as a function of the elevation angle  $\beta$  and apparent wind velocity  $v_a$ . Multiplying the  
207 angular speed of the kite with the radial coordinate  $r$  we can calculate the tangential speed  $v_{k,\tau}$ , as  
208 described by Eq. (4).

We determine the course angle of the kite by integrating the turn rate law, which is an empirical correlation between the rate of change  $\dot{\psi}$  of the heading angle (identical to the rate of change  $\dot{\chi}$  of the course angle), the apparent wind speed  $v_a$  and the relative steering action  $u_s$  [12,26,28]

$$\dot{\psi} = c_1 v_a (u_s - c_0) + \frac{c_2}{v_a} \sin \chi \cos \beta. \quad (8)$$

209 The second term in Eq. (8) quantifies the effect of gravity on the turn rate. In a next step, we combine  
210 Eqs. (2) and (4) to eliminate  $v_{k,\tau}$  and calculate the time derivatives of the azimuth and elevation angles

211 from the angular speed  $\omega$ . These derivatives are integrated to determine the angular position of the  
 212 kite.

213 To summarize, we note that the simplified kite model describes a single-input single-output  
 214 (SISO) system. The model is characterized by two position and two velocity state variables,  $(\phi, \beta)$  and  
 215  $(\omega, \chi)$ , respectively, three steering parameters  $(c_0, c_1, c_2)$  and one relative steering action  $u_s$ .

## 216 2.2. Flight path planner (FPP)

217 The purpose of the FPP is to design a suitable flight trajectory for a pumping cycle. The path  
 218 is constructed in the  $\phi$ - $\beta$  space as a sequence of connected line segments on the small earth. As  
 219 consequence, a finite state diagram can be used to describe the flight control of the kite. The states  
 220 of the high-level controller required for automated power production are explained in Figs. 4 and 5.  
 221 For the remainder of this paper our focus will be on the figure-of-eight maneuvers during the traction  
 phase.

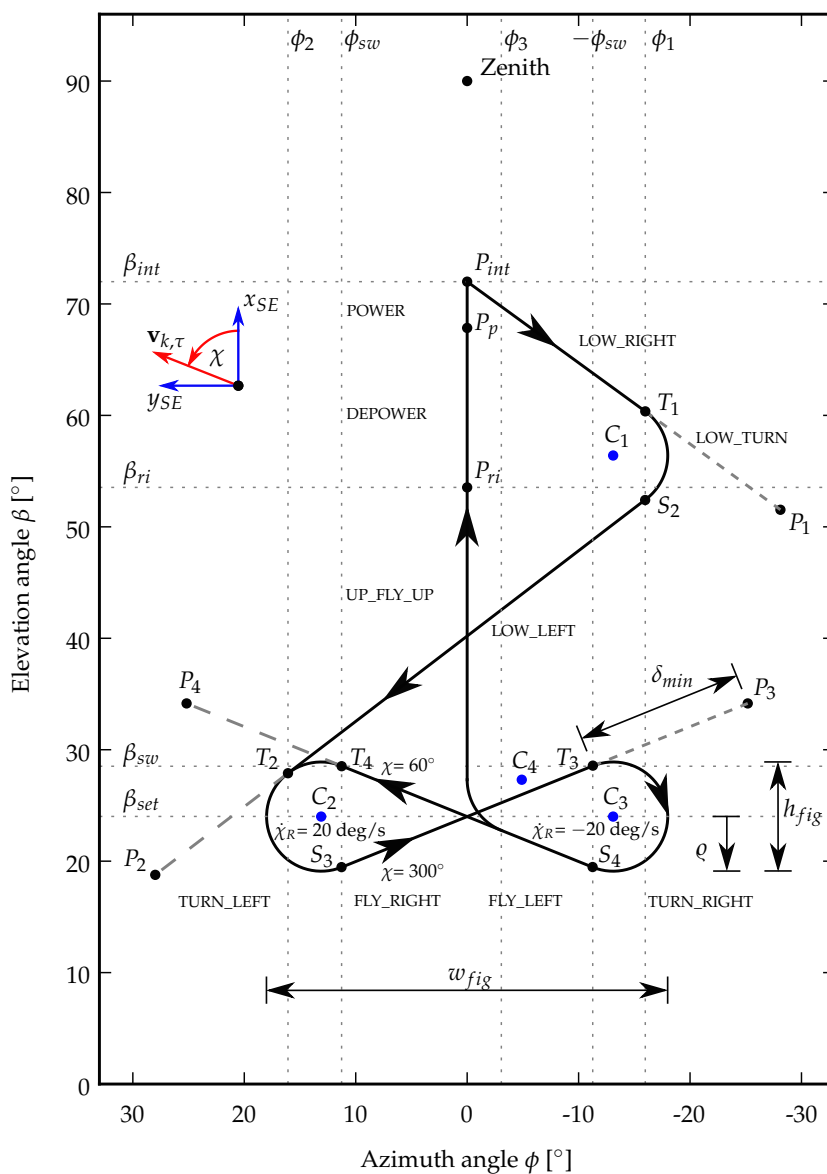


**Figure 4.** FPP for the entire pumping cycle, including the four-step planner for down-loop figure-of-eight maneuvers: First, turn left, then steer towards attractor point  $P_3$ , then turn right and finally steer towards attractor point  $P_4$  [12].

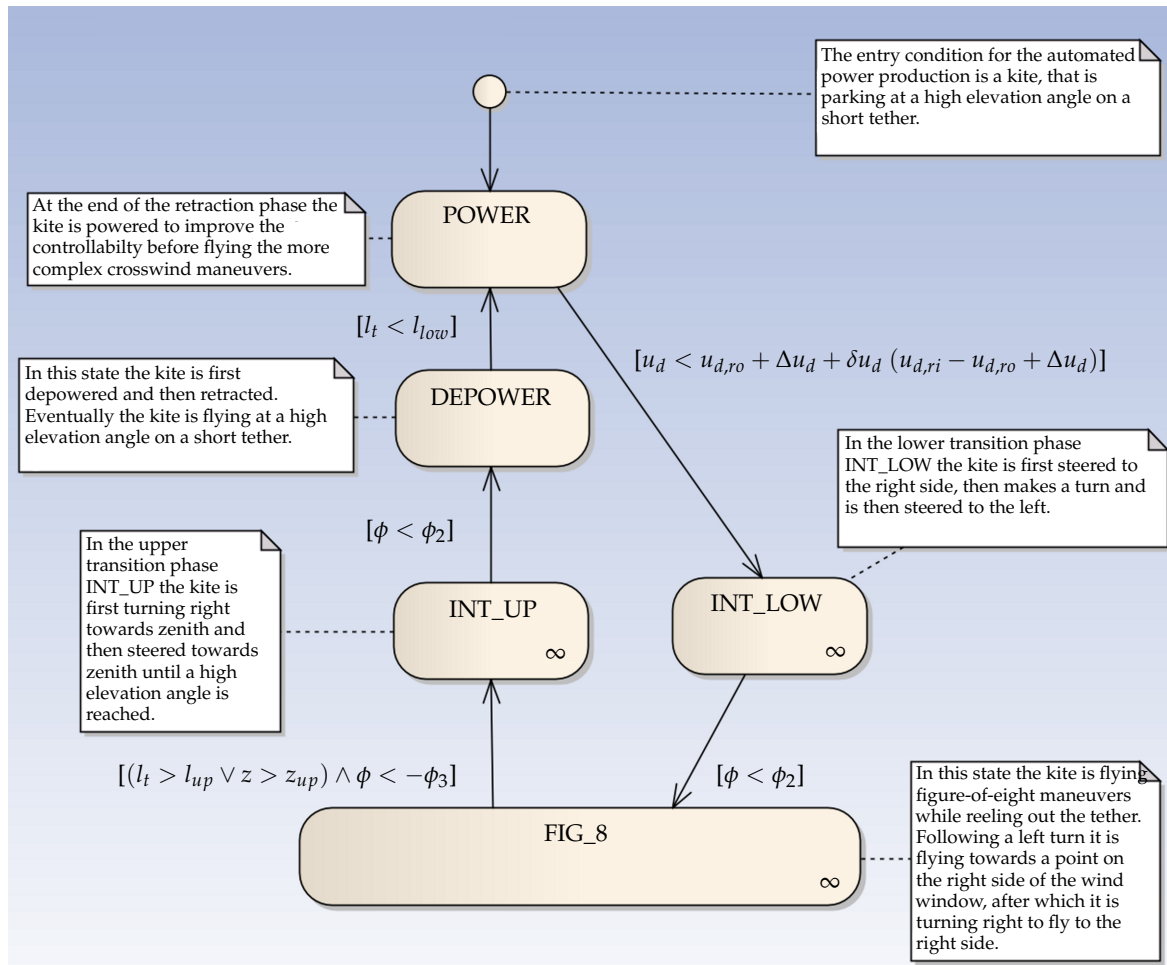


**Figure 5.** Finite state diagram for the states of high level controller for full automated power production.

223 The downloop<sup>1</sup> flight maneuvers are constructed in four steps, as shown in Table 1 and Fig. 6.  
 224 The flight maneuver starts from the initial position of the kite with a left turn (substate TURN\_LEFT).  
 225 During the turn, the set value  $\dot{\chi}_{set} = \dot{\chi}_R$  computed from the turn rate law given by Eq. (8) is used.  
 226 When reaching the switch condition  $\chi > 300^\circ - \delta_\chi$  the turning maneuver is stopped and the kite  
 227 starts flying to the right towards the attractor point  $P_3$  (substate FLY\_RIGHT). On this segment of the  
 228 figure-of-eight, the kite is steered by the PID controller, as described in Sect. 2.3. A relatively large offset  
 229 of  $\delta_\chi \approx 112^\circ$  is needed to compensate for the time delay  $\delta_t \approx 2$  s between the command to stop turning  
 230 and the kite actually stopping to turn [12]. For clarity of illustration we use in Figs. 4 and 7 a value  
 231 of  $\delta_\chi = 0$  such that the circular path segments with constant turn rate  $\dot{\chi}_R$  directly connect with the  
 232 straight path segments with constant course angle  $\chi$ . When reaching the switch condition  $\phi < -\phi_{sw}$   
 233 the kite starts a right turn (substate TURN\_RIGHT). During the turn, the set value  $\dot{\chi}_{set} = \dot{\chi}_R$  computed  
 234 from the turn rate law is used. When reaching the switch condition  $\chi < 60^\circ + \delta_\chi$  the turning maneuver  
 235 is stopped and the kite starts flying to the left towards the attractor point  $P_4$  (substate FLY\_LEFT). On  
 236 this segment of the figure-of-eight, the kite is again steered by the PID controller. When reaching the  
 237 switch condition  $\phi > \phi_{sw}$  a new figure-of-eight maneuver is started with the kite entering a left turn  
 238 (substate TURN\_LEFT).

<sup>1</sup> We distinguish between downloops and uploops depending on the direction of flight during the turning maneuvers along the outer parts of the figure-of-eight. While downloops lead to a more equalized power profile during the traction phase, uploops are generally considered to be more safe.

State	Next state	$P_{k,set}^{SE}$	$\dot{\chi}_{set}$	Switch condition
Initial	TURN_LEFT	–	$\dot{\chi}_R$	ALWAYS
TURN_LEFT	FLY_RIGHT	$P_3$	from PID	$\chi > 300^\circ - \delta_\chi$
FLY_RIGHT	TURN_RIGHT	–	$-\dot{\chi}_R$	$\phi < -\phi_{sw}$
TURN_RIGHT	FLY_LEFT	$P_4$	from PID	$\chi < 60^\circ + \delta_\chi$
FLY_LEFT	TURN_LEFT	–	$\dot{\chi}_R$	$\phi > \phi_{sw}$

**Table 1.** Finite sub-states of the figure-of-eight flight path planner [28]. The set value  $P_{k,set}^{SE}$  for the position is used only when the PID controller is active. The set value  $\dot{\chi}_{set}$  for the turn rate is used only when the PID is inactive.

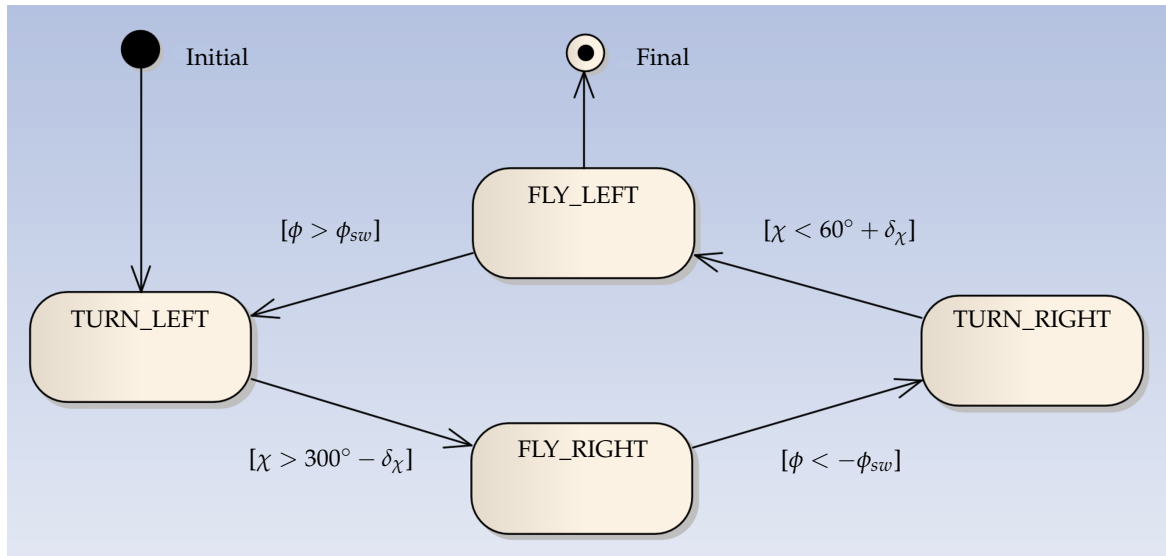


**Figure 6.** Finite sub-state diagram showing the sub-state and the transitional condition of the figure-of-eight controller.

The geometry of the figure-of-eight flight path is defined as illustrated in Fig. 4 by the angular width  $w_{fig}$  and height  $h_{fig}$ , the minimal attractor point distance  $\delta_{min}$ , defined as the arc length on the unit sphere between the kite position and the current attractor point at which the kite stops flying towards this attractor point and starts to make a turn. If the aforementioned parameters are specified, then  $P_3$ ,  $P_4$ ,  $\dot{\chi}_R$  and  $\phi_{sw}$  can be calculated by the FPP. The motion of the kite along the planned trajectory is described by the tangential velocity of the kite  $v_{k,\tau}$ , defined by Eq. (2), and the turning radius, defined as

$$q = \frac{h_{fig}}{2}. \quad (9)$$

The rate of change  $\dot{\chi}_R$  of the course angle required to fly a turn with radius  $R$  is calculated as

$$\dot{\chi}_R = \frac{v_{k,\tau}}{R} = \frac{\omega r}{R}, \quad (10)$$

where the angular velocity  $\omega$  of the kite with respect to the origin is given by Eq. (6). We note that the turning radius  $q$  as defined by Eq. (9) is an arc length on the unit sphere, while the radius of curvature  $R$  as used in Eq. (10) is a distance in Cartesian space. For practically relevant figure-of-eight maneuvers with small turning radius we can use the following approximation

$$q = \frac{R}{r}. \quad (11)$$

The value of  $\phi_{c2}$  can be calculated from

$$\phi_{c2} = \frac{w_{fig}}{2} - \varrho. \quad (12)$$

Then, the switch values  $\phi_{sw}$  and  $\beta_{sw}$  of the azimuth and elevation angles can be calculated from Eqs. (13) and (14) by combining the circle segment of the left turn with the tangent. Figure 7 illustrates

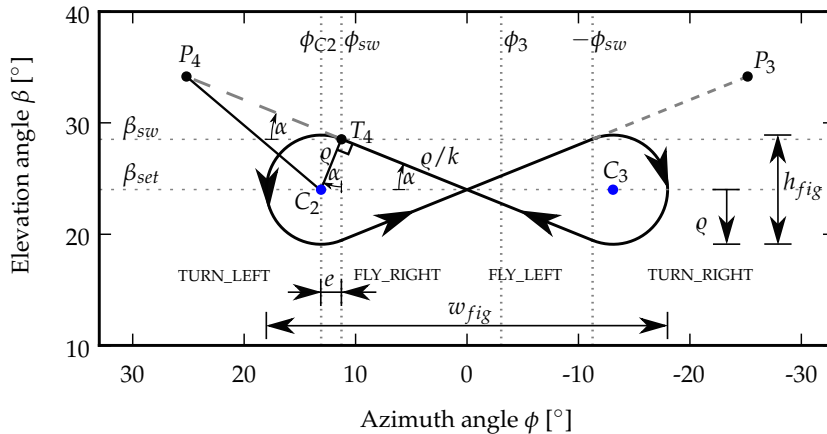


**Figure 7.** Illustrating the derivation of Eqs. (13) to (17).

the derivation of the following equations using simple geometrical relations

$$\phi_{sw} = \phi_{c2} - \frac{\varrho^2}{\phi_{c2}}, \quad (13)$$

$$\beta_{sw} = \sqrt{\varrho^2 - (\phi_{sw} - \phi_{c2})^2} + \beta_{set}. \quad (14)$$

The slope of the line towards  $P_4$  can be calculated from

$$k = \sqrt{\frac{\phi_{c2} - \phi_{sw}}{\phi_{sw}}}. \quad (15)$$

Solving for the attractor points  $P_3$  and  $P_4$ , we obtain

$$P_3 = \left( -\phi_{sw} - \delta_{\min} \sqrt{\frac{1}{1+k^2}}, \quad \beta_{sw} + \delta_{\min} k \sqrt{\frac{1}{1+k^2}} \right), \quad (16)$$

$$P_4 = \left( \phi_{sw} + \delta_{\min} \sqrt{\frac{1}{1+k^2}}, \quad \beta_{sw} + \delta_{\min} k \sqrt{\frac{1}{1+k^2}} \right). \quad (17)$$

### 239 2.3. Flight path control (FPC)

The FPC uses the attractor points  $P_3$  and  $P_4$  to guide the kite during the FLY\_RIGHT and FLY\_LEFT substates of the figure-of-eight maneuver. The required course angle  $\chi_{set}$  is calculated from the set values of the elevation and azimuth angles using great circle navigation [32]

$$y_k = \sin(\phi_{set} - \phi) \cos \beta_{set}, \quad (18)$$

$$x_k = \cos \beta \sin \beta_{set} - \sin \beta \cos \beta_{set} \cos(\phi_{set} - \phi), \quad (19)$$

$$\chi_{set} = \text{atan2}(-y_k, x_k). \quad (20)$$

240 Since the kite model is designed as a SISO system, it has just one error signal that comes from the  
 241 difference between the actual course angle of the kite, determined by integration of Eq. (8), and the  
 242 set value for the course angle given by Eq. (20). This error signal is fed into a PID controller, which  
 243 uses the relative steering input  $u_s$  to align the tangential velocity of the kite with the planned flight  
 244 direction.

245 The kite is steered along the turns of the figure-of-eight maneuver using a feed-forward controller  
 246 with the set value  $\dot{\chi}_{set} = \dot{\chi}_R$ , computed from the turn rate law given by Eq. (8), to fly a turn with radius  
 247  $R$  (or  $\rho$  in  $\phi$ - $\beta$  space). This set value is used as input of a nonlinear dynamic inversion (NDI) block to  
 248 calculate the relative steering action  $u_s$  that is required to fly the respective turn. The functions used by  
 249 the NDI block are detailed in [12].

### 250 3. System identification (SI) using Plackett's algorithm

251 The aim of the SI algorithm is to estimate the system parameters during automatic flight using  
 252 sensor data. Therefore, it is required to update the parameters in real time by analyzing the history  
 253 of the control action  $u_s$  and the course angle  $\chi$  [28]. There are several techniques for SI. In this paper  
 254 we use Plackett's algorithm [29,30] as a technique to update the dynamics of the system. This specific  
 255 algorithm has the advantage of rapidly acquiring the system parameters, without iterations, has no  
 256 singularity and the implementation on a micro-controller is simple and can be used for real-time  
 257 processing for flight tests.

The algorithm is built based on the minimization of the mean square error (MSE) of the course  
 angle  $\chi$  as defined by

$$MSE = \frac{1}{k} \sum_{r=1}^k (Y_r - Y_{m,r})^2, \quad (21)$$

258 where  $k$  is total number of time steps in the discrete time process,  $Y_{m,r}$  is the measured data for time  
 259 step  $r$  and  $Y_r$  the estimated value determined by the SI algorithm. The open-loop transfer function (TF)  
 260 of the kite is derived in [28] and it was used as a case study. The control action  $u_s$  will be denoted as  
 261  $U(z^{-1})$  and the course angle  $\chi$  will be denoted as  $Y(z^{-1})$ . The block diagram of the SI algorithm and  
 adaptive control system is illustrated in Fig. 8.

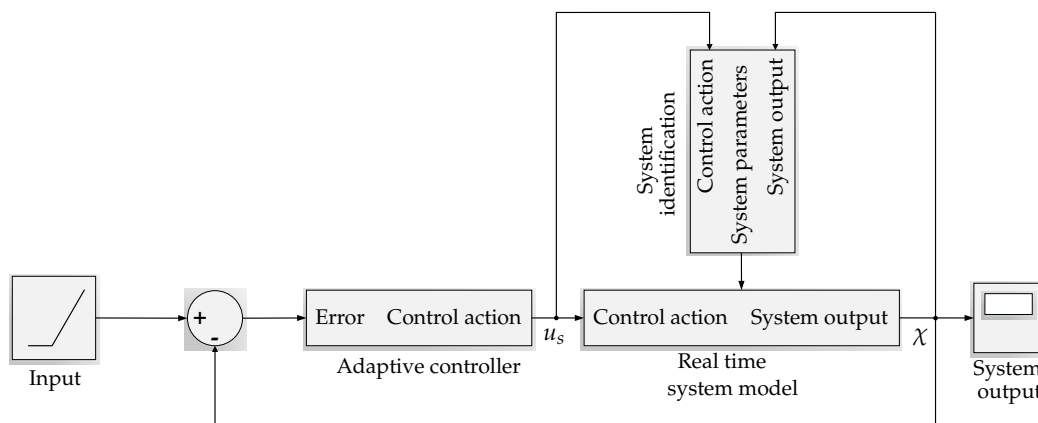


Figure 8. Block diagram of the SI algorithm and adaptive control system.

262 The SI algorithm will predict the estimated course angle  $\chi$  and update the coefficients of the  
 263 open-loop TF  $a_1, a_2, b_1$  and  $b_2$ , after that the adaptive control will update its gains based on the  
 264 parameters of the open-loop TF to stabilize the kite as described in Sect. 4. The data discussed in  
 265 Subsects. 5.1 and 5.2 considered the course angle resulted from the model in Sect. 2 as a measured  
 266 course angle. This angle was used with the steering values of the motor to calculate the estimated  
 267 course angle of the two flight conditions 5.1 and 5.2. Finally, the comparison between the results of  
 268

the simplified model control by PID controller and the adaptive control are discussed in Subjects. 5.1 and 5.2.

The SI algorithm was implemented in different way in Sect. 6.2. It utilized the measured course obtained from the real flight test of V3 kite by the TU Delft research group, not from the simplified model in Sect. 2, and the relative steering from the motor to identify the coefficients of the open loop TF without developing any controller algorithms. The open-loop TF for the kite in  $z$ -form [33] can be approximated as

$$G(z^{-1}) = \frac{Y(z^{-1})}{U(z^{-1})} = \frac{B(z^{-1})}{A(z^{-1})}, \quad (22)$$

where  $A(z^{-1})$  and  $B(z^{-1})$  are considered as second order polynomial equations in  $z$ -form

$$A(z^{-1}) = 1 + a_1z^{-1} + a_2z^{-2}, \quad (23)$$

$$B(z^{-1}) = b_1z^{-1} + b_2z^{-2}. \quad (24)$$

The coefficients  $a_1, a_2, b_1$  and  $b_2$  are varying with time because of the change in the system dynamics. The kite is also exposed to a time-varying apparent wind speed which is not available in real time. Substituting Eqs. (23) and (24) into Eq. (22), we obtain

$$\frac{Y}{U}(z^{-1}) = G(z^{-1}) = \frac{b_1z^{-1} + b_2z^{-2}}{1 + a_1z^{-1} + a_2z^{-2}}. \quad (25)$$

This equation can be rewritten in difference form

$$Y_k = -a_1Y_{k-1} - a_2Y_{k-2} + b_1U_{k-1} + b_2U_{k-2}, \quad (26)$$

or reformulated as a matrix expression

$$Y_k = \mathbf{X}_{k-1}^\top \boldsymbol{\theta}_{k-1}, \quad (27)$$

where

$$\mathbf{X}_{k-1} = [Y_{k-1}, Y_{k-2}, U_{k-1}, U_{k-2}]^\top, \quad (28)$$

$$\boldsymbol{\theta}_{k-1} = [-a_1, -a_2, b_1, b_2]^\top. \quad (29)$$

From Eq. (21), the MSE can be written as

$$MSE = \frac{1}{k} \sum_{r=1}^k \left( \mathbf{X}_{r-1}^\top \boldsymbol{\theta}_{r-1} - Y_{m,r} \right)^2. \quad (30)$$

The objective of the SI algorithm is to obtain the values of the coefficient matrix  $\boldsymbol{\theta}$  that minimize the MSE. From the derivation, these values can be calculated as

$$\boldsymbol{\theta}_k = \mathbf{P}_k \sum_{r=1}^k \mathbf{X}_{r-1} Y_{m,r}, \quad (31)$$

where  $\mathbf{P}_{k-1}$  is a square matrix such that

$$\mathbf{P}_{k-1} = \left[ \sum_{r=1}^k (\mathbf{X}_{r-1} \mathbf{X}_{r-1}^\top) \right]^{-1}. \quad (32)$$

From Eq. (32) we obtain

$$\mathbf{P}_k^{-1} = \mathbf{P}_{k-1}^{-1} + \left( \mathbf{X}_{k-1} \mathbf{X}_{k-1}^\top \right). \quad (33)$$

Equation (31) is now rewritten as

$$\boldsymbol{\theta}_k = \mathbf{P}_k \left[ \mathbf{X}_{k-1} Y_{m,k} + \sum_{r=1}^{k-1} (\mathbf{X}_{r-1} Y_{m,r}) \right]. \quad (34)$$

From Eqs. (34) and (31) we find

$$\boldsymbol{\theta}_k = \mathbf{P}_k \mathbf{X}_{k-1} Y_{m,k} + \mathbf{P}_k \mathbf{P}_{k-1}^{-1} \boldsymbol{\theta}_{k-1}. \quad (35)$$

Equation (33) can be rewritten as

$$\mathbf{P}_{k-1}^{-1} = \mathbf{P}_k^{-1} - \left( \mathbf{X}_{k-1} \mathbf{X}_{k-1}^\top \right). \quad (36)$$

Substituting Eq. (36) into Eq. (35), we obtain

$$\boldsymbol{\theta}_k = \boldsymbol{\theta}_{k-1} + \mathbf{P}_k \mathbf{X}_{k-1} \left( Y_{m,k} - \mathbf{X}_{k-1}^\top \boldsymbol{\theta}_{k-1} \right). \quad (37)$$

In Eq. (37), the term  $\mathbf{P}_k$  is unknown, thus we can apply the Lemma formula [34] to Eq. (36) to arrive at

$$\mathbf{P}_k = \mathbf{P}_{k-1} - \frac{\mathbf{P}_{k-1} \mathbf{X}_{k-1} \mathbf{X}_{k-1}^\top \mathbf{P}_{k-1}}{1 + \mathbf{X}_{k-1}^\top \mathbf{P}_{k-1} \mathbf{X}_{k-1}}. \quad (38)$$

Finally, we substitute Eq. (38) into Eq. (37) to obtain

$$\boldsymbol{\theta}_k = \boldsymbol{\theta}_{k-1} - \frac{\mathbf{P}_{k-1} \mathbf{X}_{k-1}}{1 + \mathbf{X}_{k-1}^\top \mathbf{P}_{k-1} \mathbf{X}_{k-1}} \left( \mathbf{X}_{k-1}^\top \boldsymbol{\theta}_{k-1} - Y_{m,k} \right). \quad (39)$$

271 Thus, the unknown parameters  $a_1, a_2, b_1$  and  $b_2$  have to be calculated in every time step as  $\boldsymbol{\theta}_k =$   
 272  $[-a_{1,k} \quad -a_{2,k} \quad b_{1,k} \quad b_{2,k}]^\top$  to update the estimated course angle  $\chi$  given in Eq. (26). The following  
 273 calculation steps are required to obtain these parameters. First, the matrix  $\mathbf{P}_{k-1}$  is initialized with large  
 274 positive numbers on the leading diagonal and zeros on the off-diagonal elements. The matrix  $\boldsymbol{\theta}_{k-1}$   
 275 must be populated with initial parameters close to the model. Then, the simulation results of the SI  
 276 algorithm are obtained by:

- 277 1.  $\mathbf{X}_k$  is updated every sample time by the system outputs and inputs as defined before.
- 278 2. Calculate  $\boldsymbol{\theta}_k$  and  $\mathbf{P}_k$  from Eqs. (39) and (38), respectively.
- 279 3. Update  $\boldsymbol{\theta}_{k-1}$  and  $\mathbf{P}_{k-1}$  with  $\boldsymbol{\theta}_k$  and  $\mathbf{P}_k$ , respectively.
- 280 4. Repeat the loop for each time step.

#### 281 4. Robust pole placement controller

The aim of this section is to design an adaptive control algorithm to stabilize the simplified kite model in Sect. 2. The control gains are updated with the SI algorithm described in the previous section, which makes the controller more robust compared to the classical control technique implemented in [12]. Moreover, the controller can be simply implemented on a micro-controller and installed in the KCU for autonomous operation of the kite. The closed-loop TF of the system in  $z$ -form is defined as

$$TF(z^{-1}) = \frac{G(z^{-1})G_c(z^{-1})}{1 + G(z^{-1})G_c(z^{-1})}, \quad (40)$$

where  $G(z^{-1})$  is the open-loop TF of the system given by Eq. (22) and  $G_c(z^{-1})$  is the controller TF, as defined by

$$G_c(z^{-1}) = \frac{S(z^{-1})}{R(z^{-1})}. \quad (41)$$

Substituting Eq. (22) in Eq. (40) we obtain

$$TF(z^{-1}) = \frac{B(z^{-1})S(z^{-1})}{A(z^{-1})R(z^{-1}) + B(z^{-1})S(z^{-1})}. \quad (42)$$

The next step is to calculate the controller functions  $S(z^{-1})$  and  $R(z^{-1})$  and their order [35]. We assume that these functions can be expressed as polynomials of order  $n$

$$R(z^{-1}) = 1 + r_1z^{-1} + r_2z^{-2} + \dots + r_nz^{-n}, \quad (43)$$

$$S(z^{-1}) = s_1 + s_2z^{-1} + \dots + s_nz^{-n}. \quad (44)$$

The orders  $n_s$  and  $n_r$  of  $S(z^{-1})$  and  $R(z^{-1})$  can be calculated from Eqs. (45) and (46). They are related to the orders  $n_a$  and  $n_b$  of the open-loop TF as follows

$$n_s = n_b - 1, \quad (45)$$

$$n_r = n_a - 1. \quad (46)$$

Using the SI algorithm discussed in Sect. 3, we can rewrite Eqs. (43) and (44) as

$$R(z^{-1}) = 1 + r_1z^{-1}, \quad (47)$$

$$S(z^{-1}) = s_1 + s_2z^{-1}. \quad (48)$$

Then, the characteristic equation of the closed-loop TF can be rewritten as

$$\begin{aligned} A(z^{-1})R(z^{-1}) + B(z^{-1})S(z^{-1}) \\ = (1 + a_1z^{-1} + a_2z^{-2}) (1 + r_1z^{-1}) + (b_1z^{-1} + b_2z^{-2}) (s_1 + s_2z^{-1}) = 0. \end{aligned} \quad (49)$$

Equation (49) is the characteristic equation of the closed-loop TF. By solving this equation, we will be able to tune the system behavior, i.e. time constant and steady-state error. The orders of the controller polynomials are calculated from the order of the open-loop TF. The required characteristics of our system is to place the poles of the closed-loop TF at certain positions so as to achieve stability and robustness of the system. We introduce the following equation

$$A(z^{-1})R(z^{-1}) + B(z^{-1})S(z^{-1}) = A_m(z^{-1})A_o(z^{-1}), \quad (50)$$

282 where  $A_m(z^{-1})$  is a polynomial function that contains the controller characteristics and  $A_o(z^{-1})$  is  
 283 the polynomial function which is responsible for stabilizing the order of the equation. The controller  
 284 parameters  $r_1, s_1$  and  $s_2$  can be determined by comparing the coefficients of the same order in Eq. (50).  
 285 In our design, the poles of the closed-loop TF in the  $z$ -form are 0.974653, 0.8431642 and 0.741046.

The sampling time used during the simulation was  $\Delta t = 0.02$  s. Thus, the chosen poles can be rewritten as

$$A_m(z^{-1})A_o(z^{-1}) = (1 - 2.558863z^{-1} + 2.1688783z^{-2} - 0.6089858z^{-3}). \quad (51)$$

286 The characteristic equation of our model is a third order polynomial. We applied Jury's stability test  
 287 [36], which is similar to the Routh-Hurwitz stability criterion used for continuous time systems, and  
 288 found that all roots are located inside the unit circle, which is a condition for stability. Although  
 289 Jury's stability test can be applied to characteristic equations of any order, its complexity increases for  
 290 higher-order systems.

291 Finally, we have three unknowns  $s_1, s_2$  and  $r_1$ . By substituting Eq. (51) into Eq. (50), we obtain  
 292 three equations that we can combine into a Sylvester matrix [37] as defined in Eq. (52)

$$\begin{bmatrix} 1 & b_1 & 0 \\ a_1 & b_2 & b_1 \\ a_2 & 0 & b_2 \end{bmatrix} \begin{bmatrix} r_1 \\ s_1 \\ s_2 \end{bmatrix} = \begin{bmatrix} -2.558864 - a_1 \\ -a_2 + 2.16888 \\ -0.6089866 \end{bmatrix}. \quad (52)$$

293 The controller parameters  $r_1, s_1$  and  $s_2$  are dependent on the parameters of the SI algorithm. We will  
 294 show in the following section, that the robust pole placement controller and SI algorithm increase the  
 295 flight dynamic stability of the kite when exposed to sudden changes of the apparent wind speed.

## 296 5. Simulation results

297 In this section we present simulation results using the model and algorithms described in Sects. 2,  
 298 3 and 4. We compare the results of classical (PID) controller implemented in [12] with the adaptive  
 299 control demonstrated in 4 to show the capability of the adaptive control to increase the stability of  
 300 the kite flight, both controllers used the simplified kite model derived in Sect. 2. We investigate the  
 301 flight dynamic responses of the kite for the two wind speed signals shown in Figs. 9 and 10. Flight  
 302 condition I is discussed in Subject. 5.1, while flight condition II, which is characterized by a much  
 higher frequency, is discussed in Subject. 5.2.

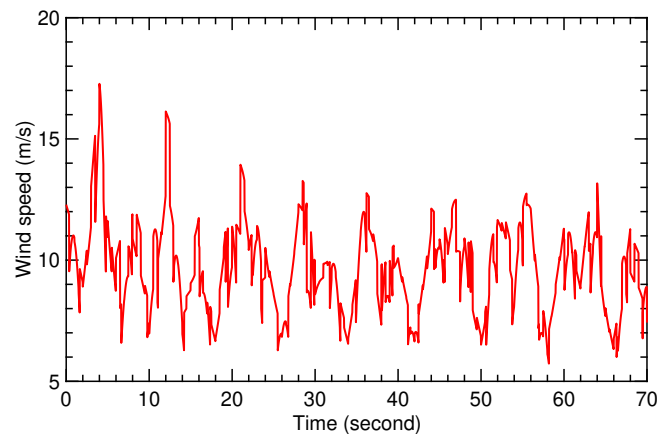


Figure 9. Time history for the wind speed during flight condition I.

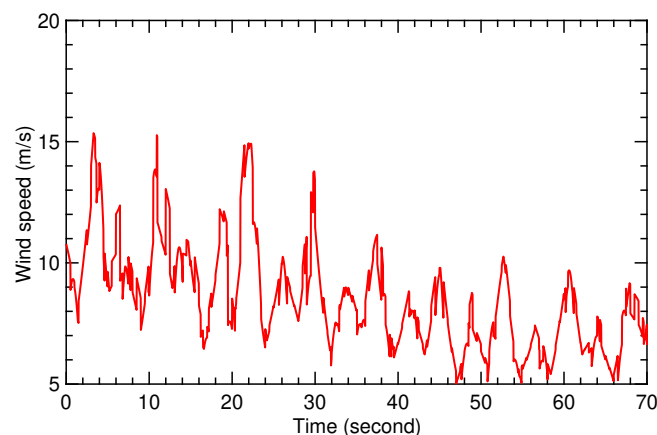


Figure 10. Time history for the wind speed during flight condition II.

303

### 304 5.1. Flight condition I

305 Flight condition I uses the wind speed illustrated in Fig. 9. The fluctuation of the wind speed  
 306 affects the flight dynamics of the kite as described by the model presented in Sect. 2. The SI algorithm

307 derived in Sect. 3 generates the values of  $a_1, a_2, b_1$  and  $b_2$  shown in Figs. 11 and 12. The resulting  
 308 figure-of-eight trajectory is illustrated in Fig. 13, calculated using the simple model and the classical  
 controller presented in Sect. 2. The figure-of-eight trajectory illustrated in Fig. 14 is calculated based

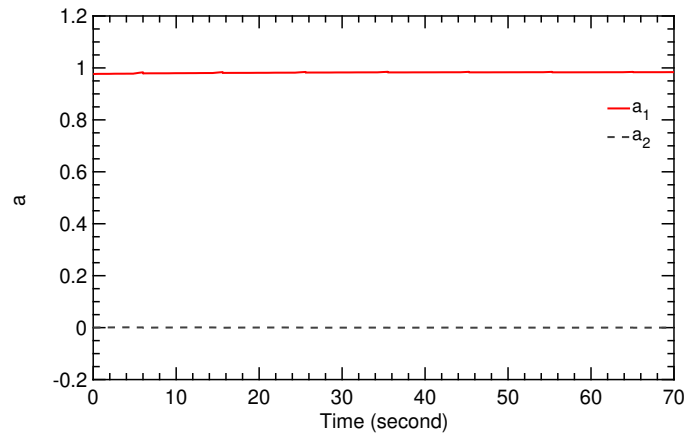


Figure 11. Time history of the SI parameters  $a_1$  and  $a_2$ .

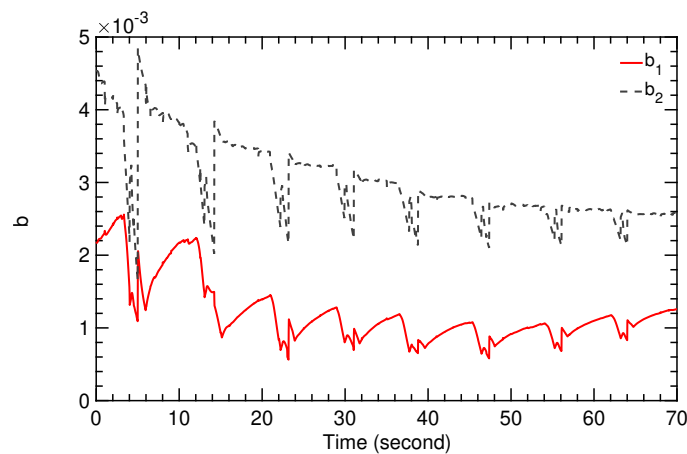


Figure 12. Time history of the SI parameters  $b_1$  and  $b_2$ .

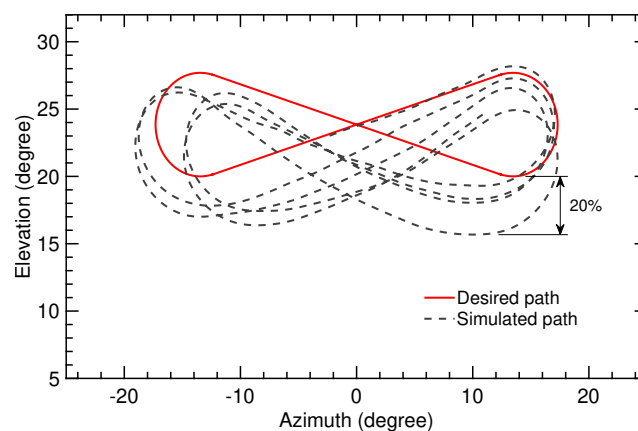
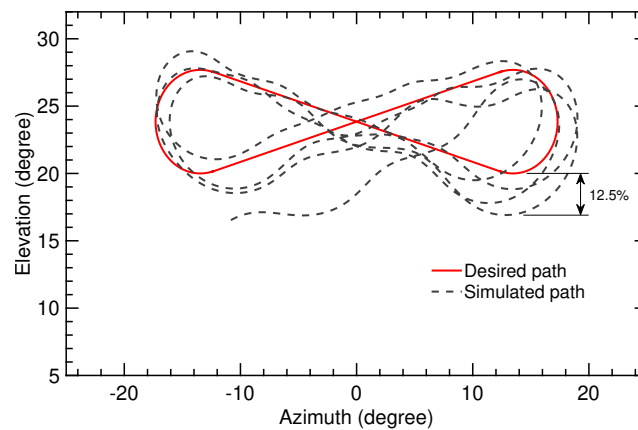
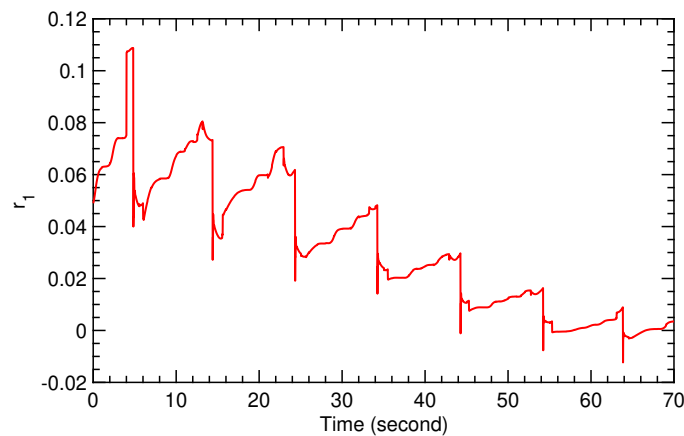


Figure 13. Trajectory computed on the basis of the classical flight controller for a flight time of 70 s.

309 on the SI algorithm and adaptive controller described in Sects. 3 and 4. The controller parameters are  
 310 updated in real time, accounting for the varying parameters  $r_1, s_1$  and  $s_2$ , as shown in Figs. 15 and  
 311 16, which in turn are updated from the varying SI parameters  $a_1, a_2, b_1$  and  $b_2$ . Figure 17 shows a  
 312



**Figure 14.** Trajectory computed on the basis of the SI algorithm and adaptive controller for a flight time of 70 s.



**Figure 15.** Time history of the controller parameter  $r_1$  for flight condition I.

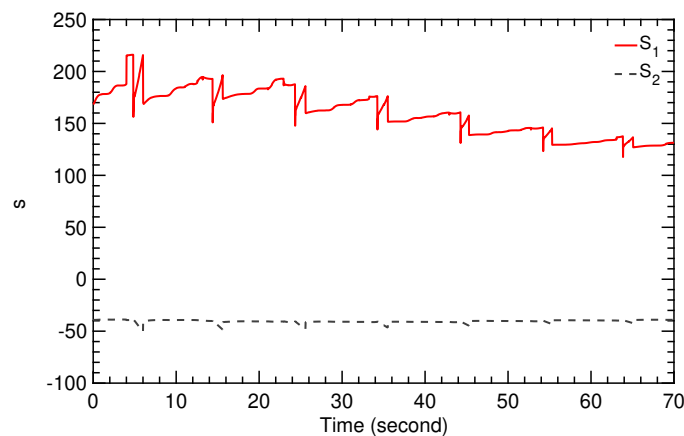


**Figure 16.** Time history of the controller parameters  $s_1$  and  $s_2$  for flight condition I.

313 very close fit between the measured course angle from the model and the estimated value from the SI  
 314 algorithm. This accuracy was achieved for a sampling time of  $\Delta t = 0.02$  s, which is very short for this  
 315 type of application.

316 To assess the tracking performance of the different control approaches we use the deviation  
 317 between the computed and the planned flight paths. From the several options to quantify this  
 318 deviation we chose the elevation angle in this study. The difference in elevation angle is a suitable  
 319 measure to quantify the operational stability of the kite because if this difference increases too much

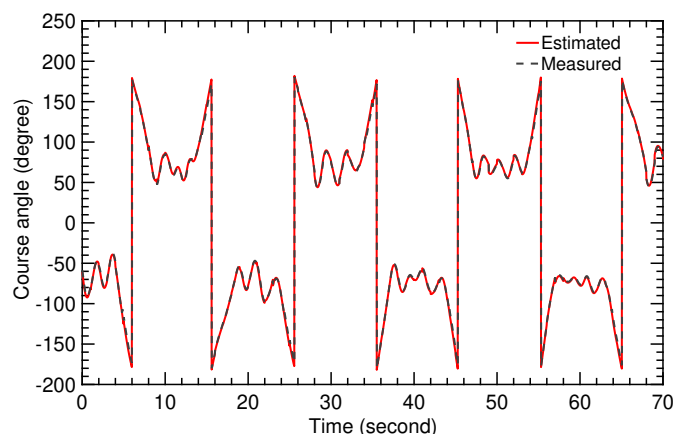


**Figure 17.** Time history of the measured and estimated values of the course angle.

320 the wing can experience aerodynamic stall. Therefore, the designed control parameters have to be  
 321 chosen carefully to keep the deviation of the elevation angle below a certain limit.

322 Figure 13 indicates that the deviation between simulated and desired paths depends on the  
 323 position along the path. We can notice that the error increases after performing the turning maneuver.  
 324 The maximum deviation for the total simulation time is  $\Delta\beta = 5^\circ$  (20%). Using the SI algorithm together  
 325 with the adaptive controller the maximum deviation is  $\Delta\beta = 2.5^\circ$  (12.5%), as depicted in Fig. 14. This  
 326 was acceptable for maintaining stable flight.

### 327 5.2. Flight condition II

328 Flight condition II uses the wind speed illustrated in Fig. 10, which is characterized by fluctuations  
 329 at much higher frequency compared to flight condition I. For this reason flight condition II is much  
 330 more demanding for the controller, which we can see from the values of the coefficients  $a_1, a_2, b_1$  and  
 $b_2$  displayed in Figs. 18 and 19. The order of the coefficients  $b_1$  and  $b_2$  in Figs. 12 and 19 is different,

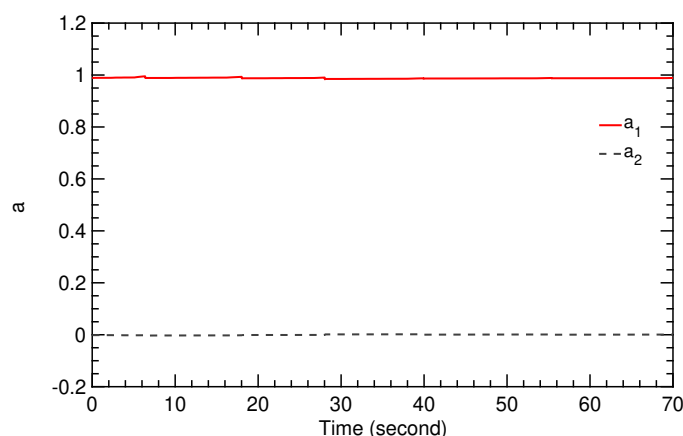


**Figure 18.** Time history of the SI parameters  $a_1$  and  $a_2$

331 because the different frequencies of the wind speed fluctuations affect the flight dynamic model of the  
 332 kite, which is then detected by the SI algorithm.

334 The computed trajectories are illustrated in Figs. 20 and 21. Figure 20 shows that the figure-of-eight  
 335 motion of the kite is progressively dropping towards lower elevation angles, while in Fig. 21 the  
 336 figure-of-eight motion stays in the vicinity of the set value  $\beta_{set} = 24^\circ$ . From this we conclude that  
 337 the classical flight controller is not capable to maintain a stable flight operation for flight condition II,  
 338 while the combination of SI algorithm and adaptive controller is capable.

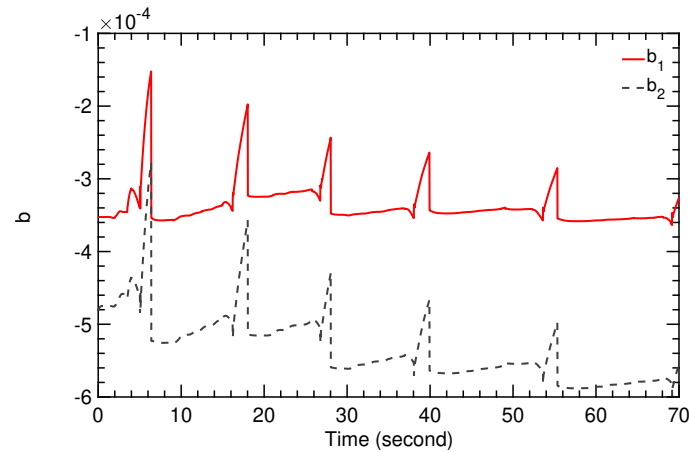


**Figure 19.** Time history of the SI parameters  $b_1$  and  $b_2$ .

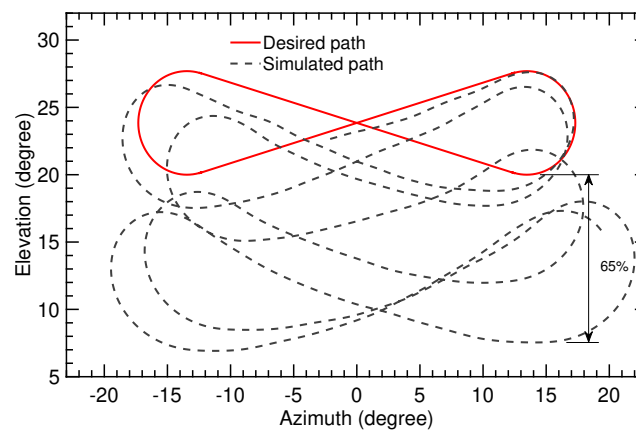


**Figure 20.** Trajectory computed on the basis of the classical flight controller for a flight time of 70 s.

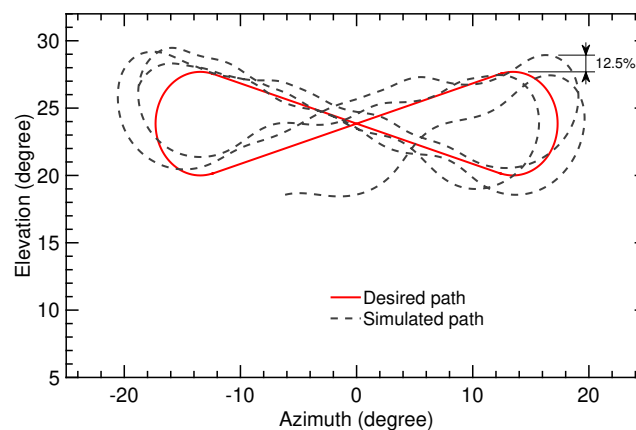


**Figure 21.** Trajectory computed on the basis of the SI algorithm and adaptive controller for a flight time of 70 s.

339 To explain why flight condition II leads to an unstable flight operation we look at the differences  
 340 of the two control approaches used in the simulation. The classical flight controller is based on a PID  
 341 controller with constant gains. While this is suitable for flight condition I, however, it can not cope  
 342 with the dynamic reaction of the model to the more rapidly fluctuating wind speed of flight condition  
 343 II. In contrast to the classical controller, the combination of SI algorithm and adaptive controller can  
 344 manage this dynamic reaction because the SI parameters  $a_1, a_2, b_1$  and  $b_2$  and controller parameters

$r_1$ ,  $s_1$  and  $s_2$  are updated in real time, as shown in Figs. 18, 19, 22 and 23, respectively. Figure 24

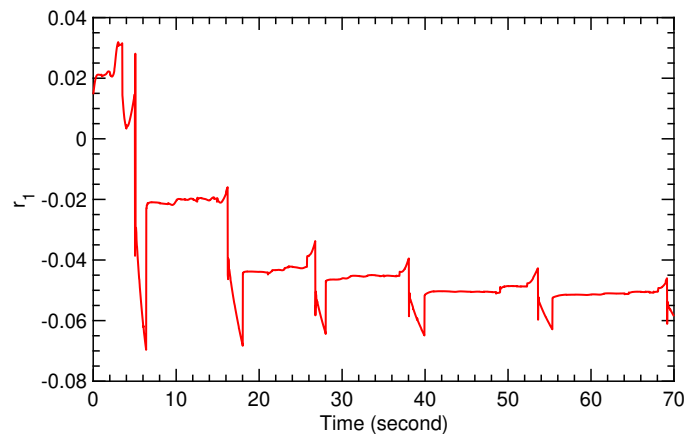


**Figure 22.** Time history of the controller parameter  $r_1$  for the flight condition II.

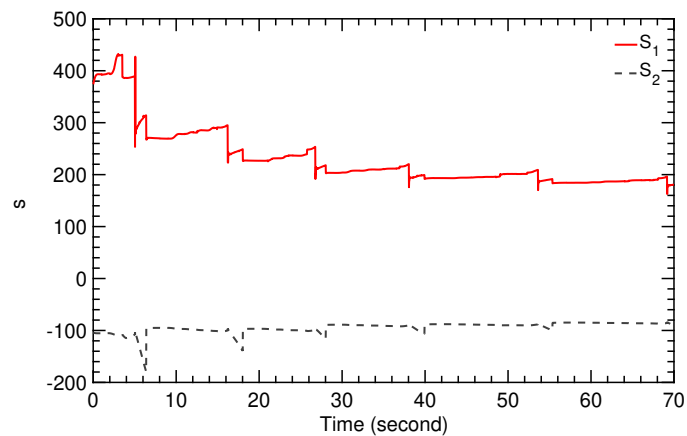


**Figure 23.** Time history of the controller parameters  $s_1$  and  $s_2$  for the flight condition II.

345

346 shows again a very close fit between the measured and estimated course angle, which demonstrates the performance of the SI algorithm for a strongly fluctuating wind speed.

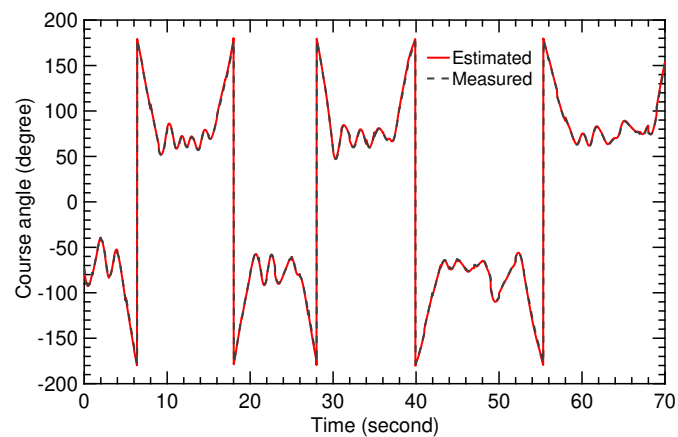


**Figure 24.** Time history of the measured and estimated course angles.

347

348 As indicated by Fig. 20, the deviation of the computed elevation angle from the planned elevation  
 349 angle increases steadily along the trajectory until reaching its maximum  $\Delta\beta = 13^\circ$  (65%) with the last  
 350 turn. This maximum deviation is three times the maximum deviation for flight condition I (see Fig. 13).

351 On the other hand, Fig. 21 shows a maximum deviation of  $2.5^\circ$  (12.5%), which is almost the same as  
 352 for flight condition I (see Fig. 14).

## 353 6. Experimental results

354 In this section we apply the SI algorithm to data that was recorded during a flight test of the  
 355 20 kW kite power system of TU Delft. The objective is to derive a mathematical model of the kite  
 356 power system directly from measurement data, omitting the use of an underlying system model with  
 357 many simplifying assumptions. As a result, the effects of the fluctuating wind velocity (magnitude  
 358 and direction) and deforming wing due to a varying aerodynamic load distribution and actuation of  
 359 the bridle line system are implicitly considered. In Subsect. 6.1 we describe the configuration of the  
 360 kite power system during the selected flight test. In Subsect. 6.2 we use the SI algorithm to derive a  
 361 mathematical model of the kite power system.

### 362 6.1. System configuration

363 The flight test was performed by the TU Delft research group on 25 October 2012 [38], using the  
 V3 kite that is illustrated in Fig. 3 and in more detail in Fig. 25. This specific kite has a total wing surface

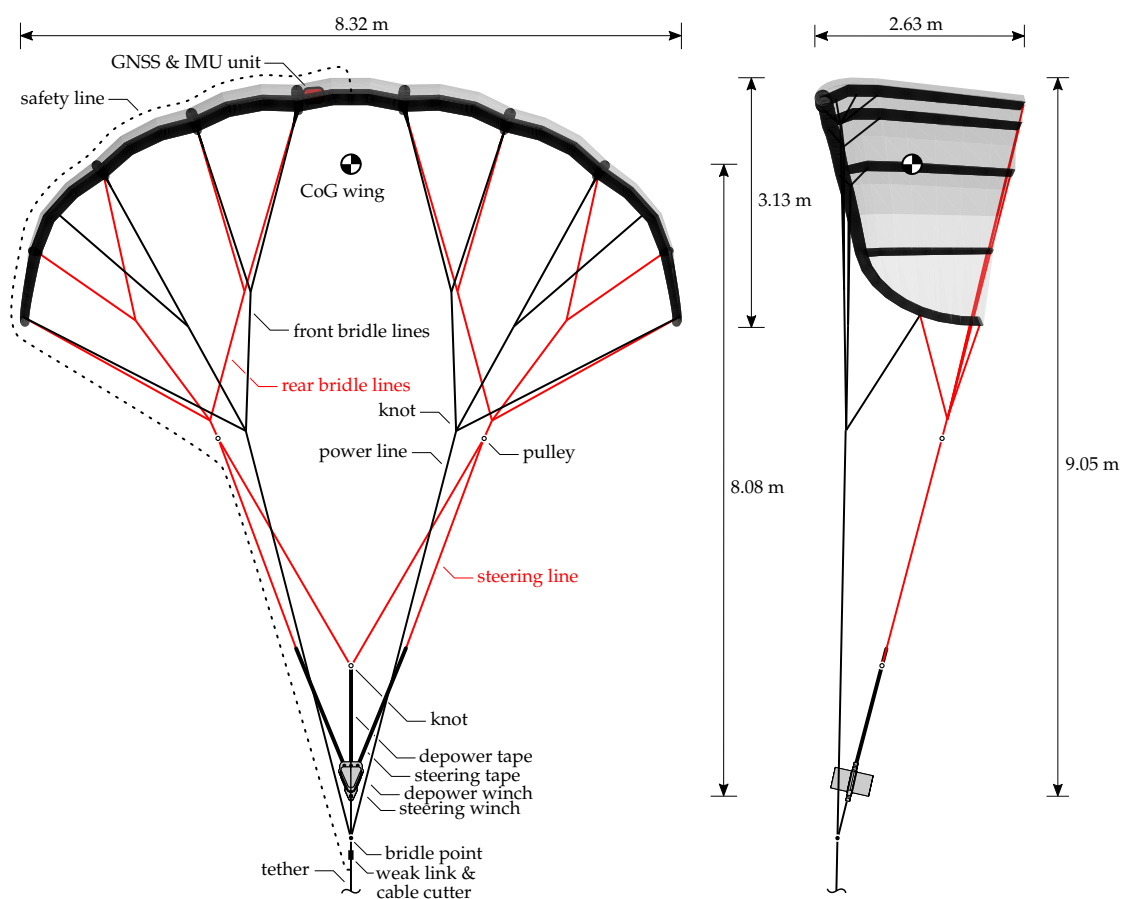


**Figure 25.** TU Delft V3 kite in front view (left) and side view (right) [38]. The KCU is displayed without the exterior foam shell and without the attached small wind turbine for supplying onboard power.

364  
 365 area of  $25 \text{ m}^2$  and is a customized and scaled up derivative of the Hydra kite, which is a commercially  
 366 available surf kite with a total wing surface area of  $14 \text{ m}^2$ . The TU Delft V3 kite consists of a flexible  
 367 membrane wing, a bridle line system and a small remote-controlled cable robot, the KCU. The wing  
 368 is designed as a leading edge inflatable (LEI) tube kite, using an inflated tubular frame to collect the  
 369 distributed aerodynamic load acting on the canopy and transmit this load to the bridle lines. The  
 370 front bridle lines directly attach to the tether, transmitting the major part of the forces, while the KCU

connects the two branches of the rear bridle lines to the tether. The integrated steering and depower winches can adjust the lengths of the steering and depower tapes to steer the wing and to adapt its angle-of-attack, respectively. The angle-of-attack is decreased during the reel-in phase to minimize the energy required to retract the kite. There are two software algorithms to control the system: the first algorithm is for maintaining figure-of-eight maneuvers during the reel-out phase while the second algorithm is for the reel-in phase. A detailed description of the different functional components of the kite power system is given in [5,9,39].

## 6.2. System identification

The results presented in this section are based on two consecutive pumping cycles that started 2615 s after launch of the kite at 15:13:41 (hh:mm:ss) [38]. Each pumping cycle consists of 110 s of tether reel-out followed by 70 s of tether reel-in. The flight motion of the kite is affected by a variety of parameters, such as the tether force, the reeling speed, the steering actuation of the KCU and the dynamics of the drum-generator module on the ground. Therefore, the SI algorithm described in Sect. 3 is used to determine the SI parameters of the kite system directly using experimental measurements. We can determine the course angle from the recorded flight data, using the attitude sensors and the relative steering action  $u_s$ . These data are sufficient for the SI algorithm to derive in real time the SI parameters  $a_1, a_2, b_1$  and  $b_2$ .

The recorded flight path of the kite for the two consecutive pumping cycles is illustrated in Figs. 26 and 27. The kite starts at an altitude of 240 m and subsequently dives down to a minimum altitude of 115 m to start a first sequence of figure-of-eight maneuvers around an average elevation angle of  $25^\circ$ . During these maneuvers the azimuth angle varies between  $-20^\circ$  and  $20^\circ$ , the tether reels out and the altitude progressively increases. After around 100 s, the figure-of-eight maneuvers are discontinued and the tether is reeled in. In this phase, the kite passes through a maximum azimuth angle of  $64^\circ$ , a maximum elevation angle of  $74^\circ$  and is climbing to a maximum altitude of 315 m before again diving down to around 115 m to start a second sequence of figure-of-eight maneuvers. Flying to large azimuth and elevation angles is a second technique to depower the kite and was used here in addition to reducing the angle-of-attack of the wing. Towards the end of the second reel-in phase the kite reaches a maximum elevation angle of almost  $60^\circ$  at a constant azimuth angle of  $-30^\circ$ , climbing to a maximum altitude of 365 m.

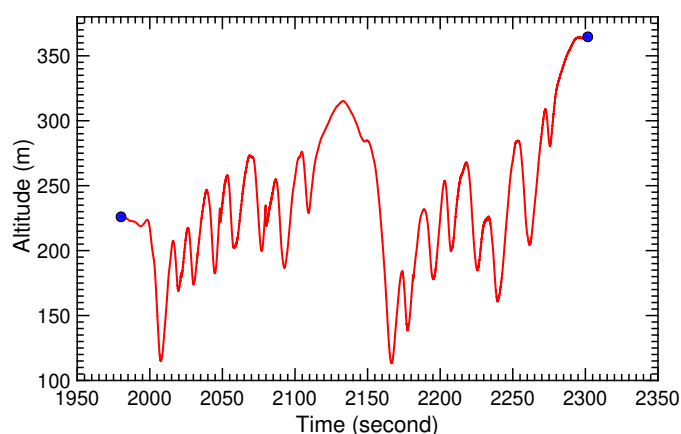


**Figure 26.** Recorded kite altitude for two pumping cycles. The origin of the time scale in this and subsequent time history diagrams is not synchronized with the launch event.

The recorded ground wind speed during the two considered pumping cycles is shown in Fig. 28, the recorded relative steering action  $u_s$  in Fig. 29 and the recorded measured course angle in Fig. 30. From these we calculate the SI parameters  $a_1, a_2, b_1$  and  $b_2$  displayed in Figs. 31 and 32. The time history diagrams reveal strong variations of the SI parameters at times 1990, 2110 and 2280 s. These variations

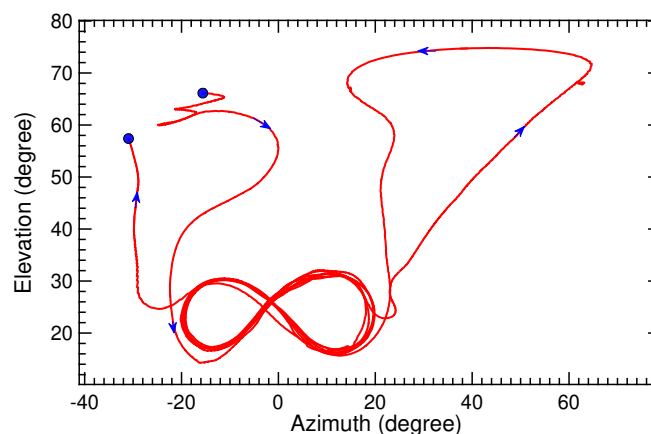


**Figure 27.** Recorded azimuth and elevation angles for two pumping cycles.

404 coincide with the transitions between reel-in and reel-out phases and demonstrate the capability of the  
 SI algorithm to adjust to the system dynamics even when rapidly changing operational modes.

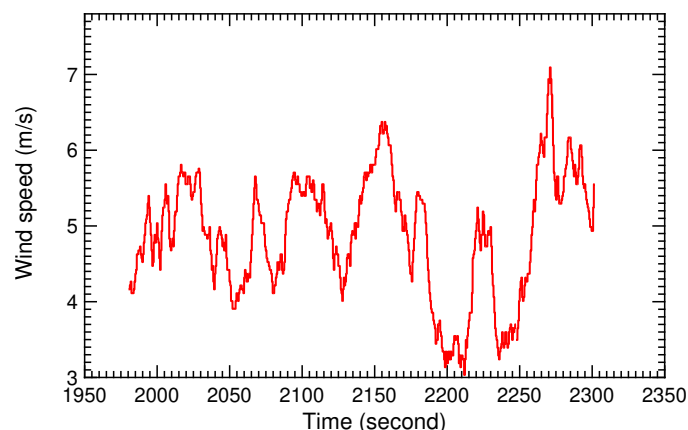


**Figure 28.** Recorded ground wind speed for two pumping cycles.

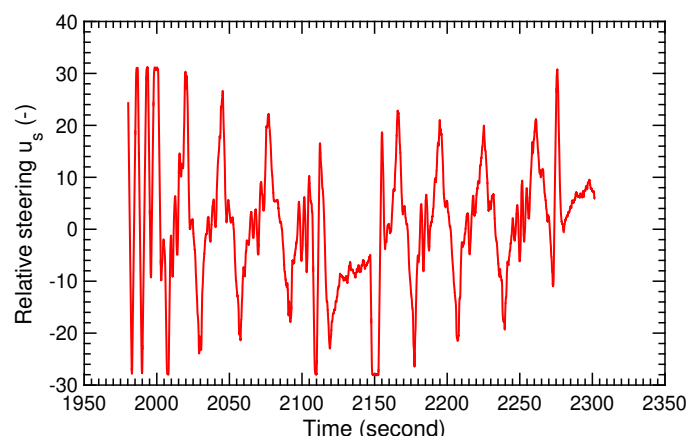


**Figure 29.** Recorded relative steering action  $u_s$  for two pumping cycles.

405

406

407

408

409

The open loop TF of the V3 kite is obtained from Eq. (25) using the calculated values of the SI parameters displayed in Figs. 31 and 32. The resulting correlation between the relative steering action  $u_s$  and the course angle  $\chi$  of the kite can be used for planning and control of autonomous flight operation. The correlation is also used in Fig. 30 to estimate the course angle using the recorded

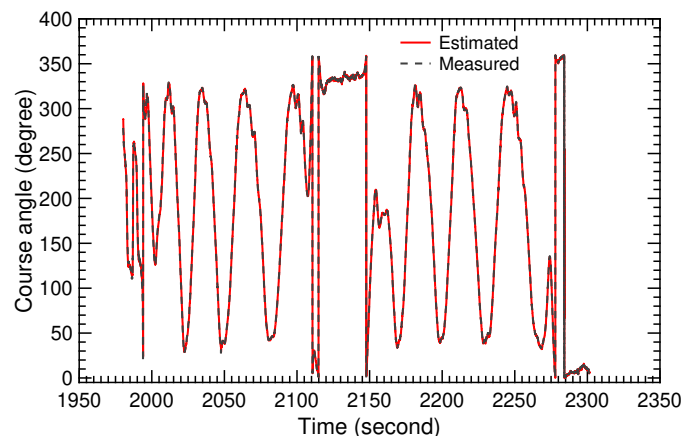


**Figure 30.** Measured and estimated course angle for two pumping cycles.

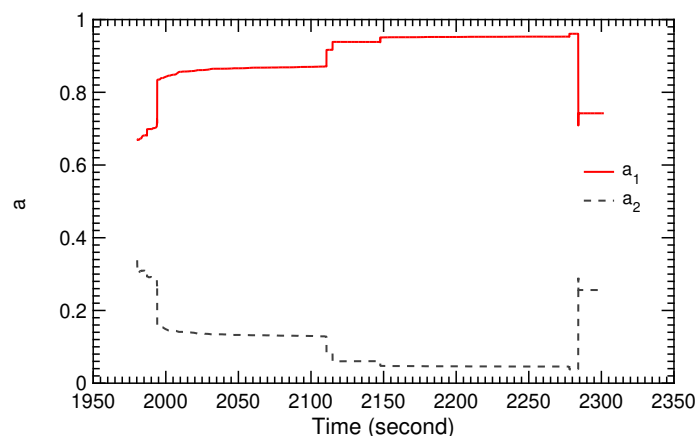


**Figure 31.** Calculated SI parameters  $a_1$  and  $a_2$  for two pumping cycles.

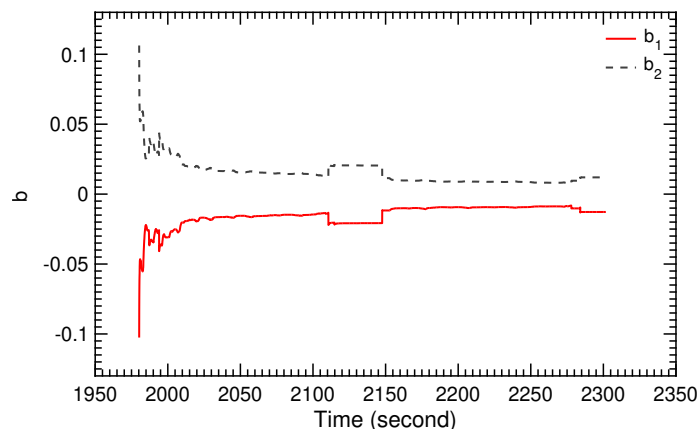


**Figure 32.** Calculated SI parameters  $b_1$  and  $b_2$  for two pumping cycles.

410 relative steering action  $u_s$  displayed in Fig. 29. The close fit between measured and estimated course  
 411 angle indicates the capability of the chosen SI algorithm to identify the system parameters without any  
 412 singularity at a very short sampling time.

413 The recorded tether force measured at the ground is shown in Fig. 33. One can clearly distinguish  
 414 the reel-out phases with an average tether force of 3000 N and the reel-in phases with an average  
 415 tether force of 700 N. The strong oscillations during the reel-out phase are induced by the figure-of-eight  
 416 motion, because the tether force is proportional to  $\cos \beta \cos \phi$  [40], and the fluctuations of the wind  
 417 speed at the position of the kite [13].

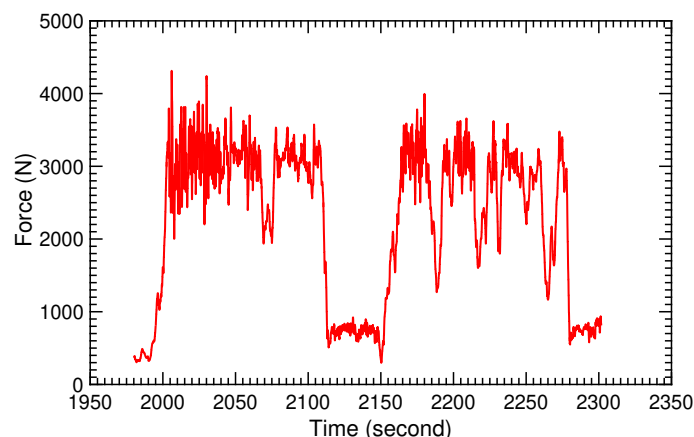


Figure 33. Recorded tether force for two pumping cycles.

## 418 7. Conclusions

419 In this paper, we have studied the flight control of a tethered flexible membrane kite used for  
 420 airborne wind energy harvesting in pumping cycles. Specifically, we investigated the figure-of-eight  
 421 maneuvers of the kite during the energy-generating reel-out phase. Following the development of a  
 422 simplified kite system model and a flight path planning algorithm, we have compared a classical PID  
 423 controller using fixed gains with an adaptive controller that uses a system identification algorithm to  
 424 adjust the controller parameters in real time. The performance of the two different control approaches  
 425 was assessed on the basis of two flight conditions that are characterized by different fluctuation  
 426 frequencies of the wind speed. We found that the classical control was not able to cope with the rapidly  
 427 fluctuating wind speed. On the other hand, the combination of adaptive control and SI algorithm  
 428 is more robust and can handle a more severely fluctuating wind speed and varying flight dynamic  
 429 behavior of the kite. The enhanced stability is a result of the real-time tuning of the control gains  
 430 at every integration time step to the varying SI parameters. In a second part of the study, the SI  
 431 algorithm was successfully applied to recorded measurement data of a test flight of a 20 kW kite  
 432 power system, equipped with a kite of 25 m<sup>2</sup> wing surface area. Despite the uncertainty of the wind  
 433 velocity in magnitude and direction and the dynamic response of the deformable membrane wing, it  
 434 was possible to successfully derive the SI parameters of the system for different operational phases,  
 435 such as reel-in and reel-out. The results suggest that the combination of adaptive controller and SI  
 436 algorithm is well suited for robust path control of a tethered membrane kite flying in a fluctuating  
 437 wind field and transitioning through different operational phases. As a next step for this research we  
 438 aim at the implementation of the adaptive controller with the experimental hardware to demonstrate  
 439 its performance in a flight test campaign.

## 440 Acknowledgments

441 Roland Schmehl was supported by the H2020-ITN project AWESCO funded by the European  
 442 Union's Horizon 2020 research and innovation programme under the Marie Skłodowska-Curie grant  
 443 agreement No. 642682

## 444 References

- 445 1. Ahrens, U.; Diehl, M.; Schmehl, R., Eds. *Airborne Wind Energy*; Green Energy and Technology, Springer:  
 446 Berlin Heidelberg, 2013. doi:10.1007/978-3-642-39965-7.
- 447 2. Cherubini, A.; Papini, A.; Vertechy, R.; Fontana, M. Airborne Wind Energy Systems: A review of the  
 448 technologies. *Renewable and Sustainable Energy Reviews* **2015**, *51*, 1461–1476. doi:10.1016/j.rser.2015.07.053.

- 449 3. Schmehl, R., Ed. *Airborne Wind Energy – Advances in Technology Development and Research*; Green Energy  
450 and Technology, Springer: Singapore, 2018. doi:10.1007/978-981-10-1947-0.
- 451 4. Lago, J.; Erhard, M.; Diehl, M. Warping model predictive control for application in control of a real airborne  
452 wind energy system. *Control Engineering Practice* **2018**, *78*, 65–78. doi:10.1016/j.conengprac.2018.06.008.
- 453 5. Van der Vlugt, R.; Peschel, J.; Schmehl, R. Design and experimental characterization of a pumping kite  
454 power system. In *Airborne Wind Energy*; Ahrens, U.; Diehl, M.; Schmehl, R., Eds.; Green Energy and  
455 Technology, Springer: Berlin Heidelberg, 2013; chapter 23, pp. 403–425. doi:10.1007/978-3-642-39965-7\_23.
- 456 6. Goldstein, L. Airborne wind energy conversion systems with ultra high speed mechanical power transfer.  
457 In *Airborne Wind Energy*; Ahrens, U.; Diehl, M.; Schmehl, R., Eds.; Green Energy and Technology, Springer:  
458 Berlin Heidelberg, 2013; chapter 13, pp. 235–247. doi:10.1007/978-3-642-39965-7\_13.
- 459 7. De Wachter, A. Power from the skies: laddermill takes airborne wind energy to new heights. *Leonardo*  
460 *Times: Journal of the Society of Aerospace Engineering Students VSV Leonardo da Vinci* **2010**, pp. 18–20.
- 461 8. Diehl, M.; Leuthold, R.; Schmehl, R., Eds. *The International Airborne Wind Energy Conference 2017:*  
462 *Book of Abstracts*, Freiburg, Germany, 2017. University of Freiburg | Delft University of Technology.  
463 doi:10.6094/UNIFR/12994.
- 464 9. Van der Vlugt, R.; Bley, A.; Schmehl, R.; Noom, M. Quasi-steady model of a pumping kite power system.  
465 *Renewable Energy* **2019**, *131*, 83–99. doi:10.1016/j.renene.2018.07.023.
- 466 10. Bosch, A.; Schmehl, R.; Tiso, P.; Rixen, D. Dynamic nonlinear aeroelastic model of a kite for power  
467 generation. *Journal of Guidance, Control and Dynamics* **2014**, *37*, 1426–1436. doi:10.2514/1.G000545.
- 468 11. Fechner, U.; van der Vlugt, R.; Schreuder, E.; Schmehl, R. Dynamic Model of a Pumping Kite Power System.  
469 *Renewable Energy* **2015**, *83*, 705–716. doi:10.1016/j.renene.2015.04.028.
- 470 12. Fechner, U. A Methodology for the Design of Kite-Power Control Systems. PhD thesis, Delft University of  
471 Technology, 2016. doi:10.4233/uuid:85efaf4c-9dce-4111-bc91-7171b9da4b77.
- 472 13. Fechner, U.; Schmehl, R. Flight Path Planning in a Turbulent Wind Environment. In *Airborne Wind Energy –*  
473 *Advances in Technology Development and Research*; Schmehl, R., Ed.; Green Energy and Technology, Springer:  
474 Singapore, 2018; chapter 15, pp. 361–390. doi:10.1007/978-981-10-1947-0\_15.
- 475 14. Breukels, J.; Schmehl, R.; Ockels, W. Aeroelastic Simulation of Flexible Membrane Wings based  
476 on Multibody System Dynamics. In *Airborne Wind Energy*; Ahrens, U.; Diehl, M.; Schmehl, R.,  
477 Eds.; Green Energy and Technology, Springer: Berlin Heidelberg, 2013; chapter 16, pp. 287–305.  
478 doi:10.1007/978-3-642-39965-7\_16.
- 479 15. Bosch, A.; Schmehl, R.; Tiso, P.; Rixen, D. Nonlinear Aeroelasticity, Flight Dynamics and Control  
480 of a Flexible Membrane Traction Kite. In *Airborne Wind Energy*; Ahrens, U.; Diehl, M.; Schmehl,  
481 R., Eds.; Green Energy and Technology, Springer: Berlin Heidelberg, 2013; chapter 17, pp. 307–323.  
482 doi:10.1007/978-3-642-39965-7\_17.
- 483 16. Oehler, J.; Schmehl, R. Aerodynamic characterization of a soft kite by in situ flow measurement. *Wind*  
484 *Energy Science* **2019**, *4*, 1–21. doi:10.5194/wes-4-1-2019.
- 485 17. Erhard, M.; Strauch, H. Theory and Experimental Validation of a Simple Comprehensible Model of  
486 Tethered Kite Dynamics Used for Controller Design. In *Airborne Wind Energy*; Ahrens, U.; Diehl, M.;  
487 Schmehl, R., Eds.; Green Energy and Technology, Springer: Berlin Heidelberg, 2013; chapter 8, pp. 141–165.  
488 doi:10.1007/978-3-642-39965-7\_8.
- 489 18. Fagiano, L.; Milanese, M.; Piga, D. Optimization of airborne wind energy generators. *International Journal*  
490 *of Robust and Nonlinear Control* **2012**, *22*, 2055–2083. doi:10.1002/rnc.1808.
- 491 19. Erhard, M.; Horn, G.; Diehl, M. A quaternion-based model for optimal control of an airborne wind energy  
492 system. *ZAMM-Journal of Applied Mathematics and Mechanics/Zeitschrift für Angewandte Mathematik und*  
493 *Mechanik* **2017**, *97*, 7–24. doi:10.1002/zamm.201500180.
- 494 20. Gros, S.; Zanon, M.; Diehl, M. A relaxation strategy for the optimization of Airborne Wind Energy systems.  
495 Proceedings of the 2013 European Control Conference (ECC); , 2013; pp. 1011–1016.
- 496 21. Rawlings, J.B.; Amrit, R. Optimizing process economic performance using model predictive control.  
497 In *Nonlinear Model Predictive Control. Lecture Notes in Control and Information Sciences*; Magni, L.;  
498 Raimondo, D.M.; Allgöwer, F., Eds.; Springer: Berlin Heidelberg, 2009; Vol. 384, pp. 119–138.  
499 doi:10.1007/978-3-642-01094-1\_10.
- 500 22. Winter, M.; Schmidt, E.; Silva de Oliveira, R. An open-source software platform for AWE systems. Book of  
501 Abstracts of the International Airborne Wind Energy Conference 2017; Diehl, M.; Leuthold, R.; Schmehl,

- 502 R., Eds.; , 2017; p. 140. <http://resolver.tudelft.nl/uuid:5c5d9285-059c-42c1-a805-a0f6eae31bcd>. Poster  
503 available from: [http://awec2017.com/images/posters/Poster\\_Araujo.pdf](http://awec2017.com/images/posters/Poster_Araujo.pdf).
- 504 23. Sieg, C.; Gehrman, T.; Bechtle, P.; Zillmann, U. AWESome: An Affordable Standardized  
505 Open-Source Test Platform for AWE Systems. Book of Abstracts of the International  
506 Airborne Wind Energy Conference 2017; Diehl, M.; Leuthold, R.; Schmehl, R., Eds.; , 2017; p.  
507 140. <http://resolver.tudelft.nl/uuid:63733b6f-d860-43ec-9208-9d5d75a08db0>. Poster available from:  
508 [http://awec2017.com/images/posters/Poster\\_Sieg.pdf](http://awec2017.com/images/posters/Poster_Sieg.pdf).
- 509 24. Dunker, S. Tether and Bridle Line Drag in Airborne Wind Energy Applications. In *Airborne Wind*  
510 *Energy*; Schmehl, R., Ed.; Green Energy and Technology, Springer: Singapore, 2018; pp. 29–56.  
511 doi:10.1007/978-981-10-1947-0\_2.
- 512 25. Rapp, S.; Schmehl, R. Vertical Takeoff and Landing of Flexible Wing Kite Power Systems. *Journal of*  
513 *Guidance, Control, and Dynamics* **2018**, pp. 1–15. doi:10.2514/1.G003535.
- 514 26. Fagiano, L.; Zraggen, A.U.; Morari, M.; Khammash, M. Automatic crosswind flight of tethered wings  
515 for airborne wind energy: modeling, control design and experimental results. *IEEE Transactions on Control*  
516 *System Technology* **2014**, *22*, 1433–1447. doi:10.1109/TCST.2013.2279592.
- 517 27. Alvin, K.F.; Park, K. Second-order structural identification procedure via state-space-based system  
518 identification. *AIAA Journal* **1994**, *32*, 397–406. doi:10.2514/3.11997.
- 519 28. Dief, T.N.; Fechner, U.; Schmehl, R.; Yoshida, S.; Ismaiel, A.M.; Halawa, A.M. System identification, fuzzy  
520 control and simulation of a kite power system with fixed tether length. *Wind Energy Science* **2018**, *3*, 275–291.  
521 doi:10.5194/wes-3-275-2018.
- 522 29. Plackett, R.L. Some theorems in least squares. *Biometrika* **1950**, *37*, 149–157. doi:10.2307/2332158.
- 523 30. Dutton, K.; Thompson, S.; Barraclough, B., Adaptive and self-tuning control. In *The art of control*  
524 *engineering*; Addison-Wesley Longman Publishing Co., Inc., 1997; chapter 11, pp. 560–582.
- 525 31. Jehle, C.; Schmehl, R. Applied Tracking Control for Kite Power Systems. *Journal of Guidance, Control, and*  
526 *Dynamics* **2014**, *37*, 1211–1222. doi:10.2514/1.62380.
- 527 32. Baayen, J.H.; Ockels, W.J. Tracking control with adaption of kites. *IET control theory & applications* **2012**,  
528 *6*, 82–191. doi:10.1049/iet-cta.2011.0037.
- 529 33. Burns, R. *Advanced control engineering*, 1 ed.; Butterworth-Heinemann: London, 2001.  
530 doi:10.1016/B978-0-7506-5100-4.X5000-1.
- 531 34. Hager, W.W. Updating the inverse of a matrix. *SIAM review* **1989**, *31*, 221–239. doi:10.1137/1031049.
- 532 35. Bobál, V.; Böhm, J.; Fessler, J.; Macháček, J. *Digital self-tuning controllers: algorithms, implementation and*  
533 *applications*; Springer Science & Business Media, 2006.
- 534 36. Ibrahim, D. *Microcontroller based applied digital control*; Wiley Online Library: New Delhi, India, 2006;  
535 chapter 8.
- 536 37. Lee, S.G.; Vu, Q.P. Simultaneous solutions of Sylvester equations and idempotent matrices separating the  
537 joint spectrum. *Linear Algebra and its Applications* **2011**, *435*, 2097–2109. doi:10.1016/j.laa.2010.09.034.
- 538 38. Schmehl, R.; Fechner, U. Kite power flight data 2011–2015. Data set. 4TU.Centre for Research Data, 2020.  
539 doi:10.4121/uuid:5e1fda11-9ae1-4c0a-ab31-4a2c04f70740.
- 540 39. Salma, V.; Friedl, F.; Schmehl, R. Reliability and Safety of Airborne Wind Energy Systems. *Wind Energy*  
541 **2019**. doi:10.1002/we.2433.
- 542 40. Schmehl, R.; Noom, M.; van der Vlugt, R. Traction Power Generation with Tethered Wings. In *Airborne*  
543 *Wind Energy*; Ahrens, U.; Diehl, M.; Schmehl, R., Eds.; Green Energy and Technology, Springer: Berlin  
544 Heidelberg, 2013; chapter 2, pp. 23–45. doi:10.1007/978-3-642-39965-7\_2.